OPEN

Evolution of UHF Body Imaging in the Human Torso at 7T

Technology, Applications, and Future Directions

M. Arcan Erturk, PhD, Xiufeng Li, PhD, Pierre-Fancois Van de Moortele, PhD, Kamil Ugurbil, PhD, and Gregory J. Metzger, PhD

Abstract: The potential value of ultrahigh field (UHF) magnetic resonance imaging (MRI) and spectroscopy to biomedical research and in clinical applications drives the development of technologies to overcome its many challenges. The increased difficulties of imaging the human torso compared with the head include its overall size, the dimensions and location of its anatomic targets, the increased prevalence and magnitude of physiologic effects, the limited availability of tailored RF coils, and the necessary transmit chain hardware. Tackling these issues involves addressing notoriously inhomogeneous transmit B_1 (B_1^+) fields, limitations in peak B_1^+, larger spatial variations of the static magnetic field B_0, and patient safety issues related to implants and local RF power deposition. However, as research institutions and vendors continue to innovate, the potential gains are beginning to be realized. Solutions overcoming the unique challenges associated with imaging the human torso are reviewed as are current studies capitalizing on the benefits of UHF in several anatomies and applications. As the field progresses, strategies associated with the RF system architecture, calibration methods, RF pulse optimization, and power monitoring need to be further integrated into the MRI systems making what are currently complex processes more streamlined. Meanwhile, the UHF MRI community must seize the opportunity to build upon what have been so far proof of principle and feasibility studies and begin to further explore the true impact in both research and the clinic.

Key Words: 7 Tesla, body imaging, parallel transmit, RF coils, RF shimming, ultrahigh field

(*Top Magn Reson Imaging* 2019;28:101–124)

The evolution of human torso imaging on ultrahigh field (UHF) (≥7 Tesla) magnetic resonance imaging (MRI) scanners has paralleled advances in neuroanatomical and functional imaging. However, there are unique opportunities and challenges that exist in the human torso from the heart to the prostate, which continue to necessitate the development of novel solutions.

Continued developments in acquisition methods, radiofrequency (RF) hardware, and RF management strategies have allowed significant progress to be made in MRI of the human torso at UHF (≥7.0 Tesla). Just as in the brain, UHF body imaging has benefitted from the push and pull that exists between technology developments and applications (ie, target driven needs). Continued innovation is necessary to overcome the multiple challenges, which decrease the overall benefits of using these systems both in research and the clinic. The reward for continuous and dedicated efforts on this front will be a highly sensitive tool for biomedical discovery and the potential for improved clinical diagnostics and care.

The most frequently cited advantage of UHF, which both justifies further developing the technology and establishing its safety for human investigations, is the increase in signal-to-noise ratio (SNR), which scales supralinearly with the field strength (ie, SNR $\sim B_0^{1.65}$)[1] and can be realized to be even higher (SNR $\sim B_0^2$).[2] While acquisition and anatomy-specific relaxation effects need to be accounted for, this underlying increase in SNR plays an important role in the overall benefits expected from increasing field strengths. Other significant UHF advantages include improved parallel imaging performance,[3] increased susceptibility-based contrast for improved anatomic and functional imaging,[3,4] increased chemical shift dispersion for improved spectroscopic quantification,[5,6] shifting exchange to faster regimes for improved chemical exchange saturation transfer (CEST) studies,[7] and increased longitudinal relation times for improved noncontrast-enhanced arterial spin-labeling (ASL) perfusion, in-flow angiography,[8–10] and 4D flow acquisitions.[11,12]

In order to realize these benefits, nontrivial challenges need to be overcome with the most prevalent being the transmit B_1 (B_1^+) field heterogeneities, which increase along with the size of the imaging region of interest. As the RF wavelength used in MR approaches or becomes shorter than the dimensions of the object to be imaged, significant B_1^+ field distortions occur that are dependent on tissue electromagnetic properties and geometry.[13,14] At 7T, the RF wavelength in biological tissues at the Larmor frequency (∼300 MHz) is approximately 12 cm on average; this rather short wavelength results in complex and nonuniform transmit profiles in human tissues[15,16] due to constructive and destructive interferences.[17]

In combination with B_1^+ homogeneity issues, challenges related to limitations in peak achievable B_1^+ and concerns of local heating present further issues exacerbated by the geometry and size of the human torso. Addressing these interrelated issues has involved the constant development of RF transmit chain technologies, RF management strategies, and RF coil developments each motivating the other. In contrast to lower field systems, local rather than global power deposition and heating becomes a primary limitation as governed by the International Electrotechnical Commission (IEC) guidelines.[18] Local power deposition is characterized by the specific absorption rate (SAR) given in W/kg averaged over 10 g and is estimated through electromagnetic (EM) simulations of specific RF coils in human body models. RF coil simulations are typically performed as part of a coil validation process, which is often negotiated between a site and their local regulatory agencies. An example of a comprehensive validation procedure has been described by Hoffmann et al.[19] Through the developments of all the interrelated RF technologies, transmit efficiency, homogeneity, and power deposition have been addressed in the applications presented below with further opportunities for improvement moving forward.

From the Center for Magnetic Resonance Research, University of Minnesota, Minneapolis, MN.

Received for publication February 9, 2019; accepted March 12, 2019.

Address correspondence to Gregory J. Metzger, PhD, Center for Magnetic Resonance Research, University of Minnesota Medical School, 2021 6th Street SE, Minneapolis, MN 55455 (e-mail: gmetzger@umn.edu).

Relevant funding from the author's institution, which supported some of the presented results, originated from NCI R01 CA155268, WM Keck Foundation, NIBIB P41 EB015894, S10 RR029672, S10 RR029672 and NIBIB P41 EB0227061.

Authors Erturk and Metzger are co-authors on a patent of the 16LD RF coil.

DOI: 10.1097/RMR.0000000000000202

Beyond RF-related issues, physiologic confounders are increasingly impactful and become more difficult to manage at UHF in body applications. First, motion in the torso directly competes with the goal of exploiting SNR advantages to obtain higher resolution data. Second, the linear scaling of susceptibility effects with field strength, which is beneficial in some areas such as functional MRI (fMRI), becomes a challenging issue when considering larger scale, motion-induced, temporally varying static field inhomogeneities.[20] Third, common strategies for triggering and gating are compromised at UHF. Field strength dependent magnetohydrodynamic (MHD) effects obscure the T-wave used in standard cardiac triggering[21] and standard navigator strategies can be hindered by the same RF inhomogeneities impacting image contrast.[11,12,22]

Motivated by the promise of UHF to accelerate discoveries in brain science, several preclinical and human UHF MRI systems were designed and constructed, including the first whole body 7T system installed in 1999 at the Center for Magnetic Resonance Research at the University of Minnesota. This passively shielded scanner inspired subsequent commercial efforts. While fMRI was mission number one for this scanner, imaging of the human torso was also performed.[23] From this point forward, and with increased availability of 7T systems from major manufacturers, UHF body imaging efforts have steadily grown.

Previously, several thorough reviews have detailed the challenges and opportunities of UHF torso imaging in general for the whole body[24–26] as well as more focused reviews on UHF cardiovascular[27–29] and renal applications.[8] As the field is quite broad, this review will not attempt to embody all UHF studies and developments below the neck. Notable exceptions include multinuclear applications, breast imaging, and musculoskeletal applications. It is our intention to provide a more historical perspective on torso imaging developments and how the interplay between technology developments and applications have helped the field grow and reveals the new opportunities and challenges that lay ahead.

TRANSMIT ELECTROMAGNETIC FIELDS: HARDWARE

For proton (^{1}H) imaging and spectroscopy, managing limitations in peak B_1^+, B_1^+ homogeneity and peak local SAR have driven critical advances in RF coils, transmit chain architectures, RF shimming strategies, RF pulse design, and acquisition methods necessary for UHF body imaging. Some of these critical developments are detailed below focusing on those relevant to the anatomy specific sections that follow.

Radiofrequency (RF) Coils

Initial body imaging studies demonstrated on the 4T systems were performed using a transverse electromagnetic (TEM) resonator driven by a single 8 kW RF amplifier for transmit and local receiver arrays for receive.[30] This type of whole-body RF transmitter and local receive configuration was similar to the clinical setups at 1.5T and 3.0T during the same time period. The TEM resonator was driven through 4 ports, which foreshadowed the later adoption of multichannel transmit on clinical 3T systems.[31] While similar whole-body transmitters[23,32] with local receive arrays[33,34] were originally explored for 7T, the ability to generate the B_1^+ necessary for many standard imaging sequences was not possible due to limitations in the transmit chain coupled with poor transmit efficiency of the systems. Despite these challenges, new strategies for exploring the potential of integrated whole body ^{1}H transmit RF coils continue.[35,36]

In the absence of a viable whole body proton transmitter solution, the work-horse RF coils for most UHF body imaging applications have been local transmit and receive (ie, transceiver) arrays.[37–46] The first arrays were larger scale versions of those successfully implemented for imaging the human head.[47] These close-fitting transceiver arrays, developed both independently and in collaborations by several groups, illustrate the variety of attempts that have been conducted, using different geometries and resonant structures with a continuing goal to improve transmit and/or receive performance. On the receive side, design criteria include improved sensitivity and parallel imaging performance. On the transmit side, the focus has been on decreasing peak local SAR (W/kg) and increasing transmit efficiency ($B_1^+/W^{0.5}$), SAR efficiency ($B_1^+/SAR^{0.5}$), and in combination with the RF transmit chain, peak achievable B_1^+. Recently, several groups have begun to explore and evaluate the addition of separate receive-only elements along with the transmit side technologies for body arrays.[48,49] Minimizing interferences between receive and transmit elements, maintaining acceptable transmit performance, and developing a robust, practical, and comfortable mechanical housing are among some of the challenges that need to be addressed with this approach.

Parallel Transmit Systems

The RF transmit architecture to drive the transceiver arrays used for proton body imaging impacts the methods that can be used to manage the EM fields in terms of transmit B1 and SAR management through RF shimming and RF pulse design ([50] and references therein). Initially, multichannel array coils were driven with a single RF power amplifier, which fed into multiple ports or elements using a splitter or feeding network, providing static RF shimming capabilities (by adjusting the relative phase of each transmit channel) to improve field homogeneity. Initial body imaging experiments with this approach were initially shown to be beneficial at 4T[30] (Fig. 1). To expand control over the different elements of the transceiver arrays, parallel transmit (pTx) architectures were conceived and implemented,[51] first on a 9.4T head-only system[52] and later on the first 7T whole body scanner.[23,32] The increased degrees of freedom afforded by the new pTx functionality was needed as the RF shims required to satisfy the desired transmit profile are dependent on the RF coil, the object loading the coil, and the target of interest.[53] These initial systems used a single waveform generator from the spectrometer, but that waveform was modulated channel-wise by a programmable transmit phase and magnitude (gain) controller as inputs to channel-dependent RF power amplifiers. This first version of pTx system with channel-dependent phase and magnitude control per channel will be referred to as *pTx-v1*. To supplement the standard power monitoring, additional home-grown channel-dependent monitoring hardware and software were implemented on which coil and target specific time averaged power limits could be set.[54,55] These initial parallel transmit setups provided the needed flexibility to accomplish a wide range of static RF shimming applications in the body but were still mostly beneficial for smaller and/or targeted regions of interest as detailed below.

More recently, a second version of pTx systems was developed, *pTx-v2*, and have been integrated into commercial UHF scanners where each transmit channel has its own synthesizer therefore permitting channel-dependent waveforms.[53,56] This hardware further increases the degrees of freedom available for RF shimming. The pTx-v2 systems permit dynamic RF shimming, which is differentiated from static RF shimming by the ability to modify channel specific phase and magnitude during the RF pulse at a much smaller time scale than pTx-v1 systems. To complete such systems, advanced power monitoring is typically implemented allowing real-time channel-specific complex recording of forward and reflected power permitting the real-time prediction of local SAR through the use of virtual observation points (VOPs) assuming that appropriate EM simulations had been performed for the given coil and anatomy.[57]

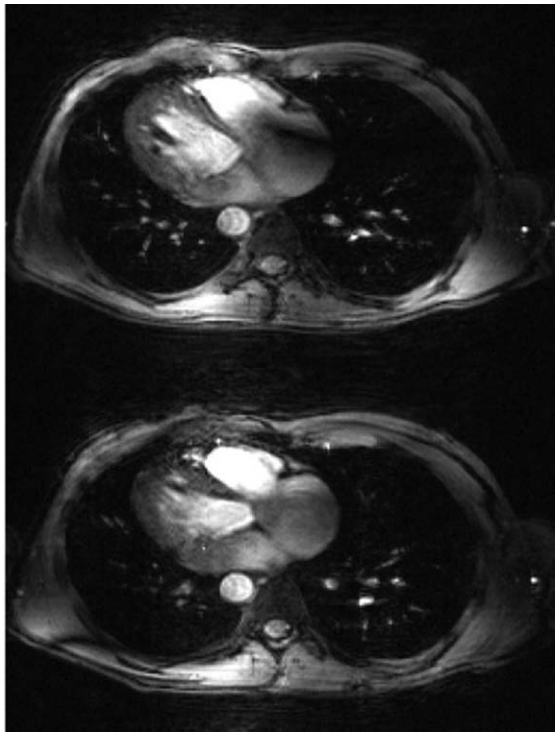

FIGURE 1. Preliminary 4T-gated cardiac images were acquired with the TEM body coil transmitter and phased-array receivers. An artifact in the right atrium common to 4T heart images (A) is corrected by RF shimming (B). Images were acquired with a 4-channel, phased-array receiver using an EKG gated gradient-echo sequence (TE 4.3 ms, slice 5 mm, FOV 40 30 cm^2, matrix 256 128). An 8-kW RF power amplifier was used to drive the transmit coil. No intensity correction was applied to these 4-loop, phased-array images. Republished with permission of John Wiley and Sons from ''Efficient high-frequency body coil for high-field MRI,'' Vaughan JT, Adriany G, Snyder CJ, et al. 2004;52(4): 851-859.

RF MANAGEMENT STRATEGIES

Static RF Shimming

Multichannel transmit arrays driven by systems with pTx RF architectures have enabled applications in targeted regions in both head[17,58] and body[59,60] by employing channel-dependent magnitude and phase RF shimming. Along with the transmit coil, the optimization strategy of choice depends on the target region's size, geometric complexity, and location. While initially performed on a single transmit system, the methods and benefits of static RF shimming were demonstrated in the body in 2008 with an 8-channel stripline transceiver array coil at 7T in the prostate.[59] The calibration methods needed for a majority of static RF shimming included tools to measure the relative complex B_1^+ from each transmit element in the transceiver array.[17,61] This method uses a low flip angle approximation to allow the robust estimation of each transmit channels spatially varying relative magnitude and phase[62,63] (Fig. 2A,B). Initial body studies at 7T required the use of a splitter, manual phase shifters, and cable lengths to implement subject-depending B_1^+ shims optimized for efficiency in the prostate.[59] However, the coil, calibration methods, and optimization strategies were applicable to and highly accelerated on systems with a pTx architecture.[54]

One tradeoff that users are always confronted with is the conflicting goals of RF efficiency and RF homogeneity, while a tradeoff solution can be sought between the two, increasing homogeneity necessarily decreases efficiency.[10] This becomes a critical issue as what is best for the sequence in terms of the imaging results or contrast must be balanced against what is practical for the system in terms of peak B_1^+ and what is safe for the subject in terms of power deposition or SAR.

Dynamic RF Shimming

Whereas static RF shimming aims at optimizing a static resultant B_1^+ field obtained by the superposition of channel-specific complex B_1^+ fields, optimized by adjusting complex channel-specific weights, dynamic RF shimming by contrast focuses on the optimization of flip angles through the optimization of channel-specific waveforms in concert with gradient waveforms. As such, dynamic RF shimming provides increased degrees of freedom not only for addressing B_1^+ inhomogeneities but also to minimize the corresponding SAR deposition. The end result is the ability to homogenize flip angles over much larger fields of view not possible with static *RF* shimming. While it is possible to implement some dynamic *RF* shimming pulses on pTx-v1 systems such as spoke pulses, the ultimate flexibility arises when pTx-v2 systems are available.

To date, a limited number of dynamic RF shimming studies have been attempted for in vivo human body applications. Examples include the homogeneous imaging of the liver[64] (Fig. 3) and efficient simultaneous multislice cine imaging of the heart[21,65,66]. The limited adoption of dynamic pTx functionality is due to a variety of factors. First, there are increased requirements for mapping B_0 and channel-dependent B_1^+ for dynamic shimming and pTx pulse design. Second, the theoretical advantages of real-time SAR monitoring to efficiently use the available RF power available have not been realized due to uncertainty in RF coil modeling and the known influence of subject-specific effects leading to the need for large, conservative safety factors when setting limits on power deposition.[42,67] Finally, the initial pTx systems have not always been robust enough to allow the rapid development and exploration of the technology, which is being resolved in next-generation systems.

Recently, in order to mitigate the necessity of acquiring extensive multichannel calibration data for dynamic RF shimming for each subject, universal pTx pulses have been proposed. [68] These pulses are pre-trained on a test population and the resultant pulse is used with new subjects without the need to acquire additional calibration data.[68] While demonstrated to be robust for head applications, further investigation is required to understand how applicable similar strategies are in the torso due to anatomical variations between target organs and individuals. In the head, while subject-specific calibrations for k_T pulse design demonstrated better normalized root mean-square error of the flip angle profiles, universal k_T pulses performed better than CP^+ and static RF shimming solutions in multislice gradient echo (GRE) imaging and 3D T1- and T2-weighted acquisitions.[68,69]

Dynamically Applied RF Shim Solutions

Some alternatives exist to the static and dynamic RF strategies described above. The first idea capitalizes on the fact that the requirements for each RF pulse in a multipulse sequence may be different. An earlier demonstration of this was in brain spectroscopy where a separate RF shim was used for localization and outer volume suppression.[70] The differences might not only vary between RF shimming requirements but also with respect to the anatomical region over which each RF pulse needs to be optimized. This idea of dynamically applied static RF shimming solutions has been successfully implemented to enable ASL[71,72], angiography[10,22] and 4D flow[11,12] studies in the human torso. In addition to managing the B_1^+ requirements of the sequences, this strategy has the added

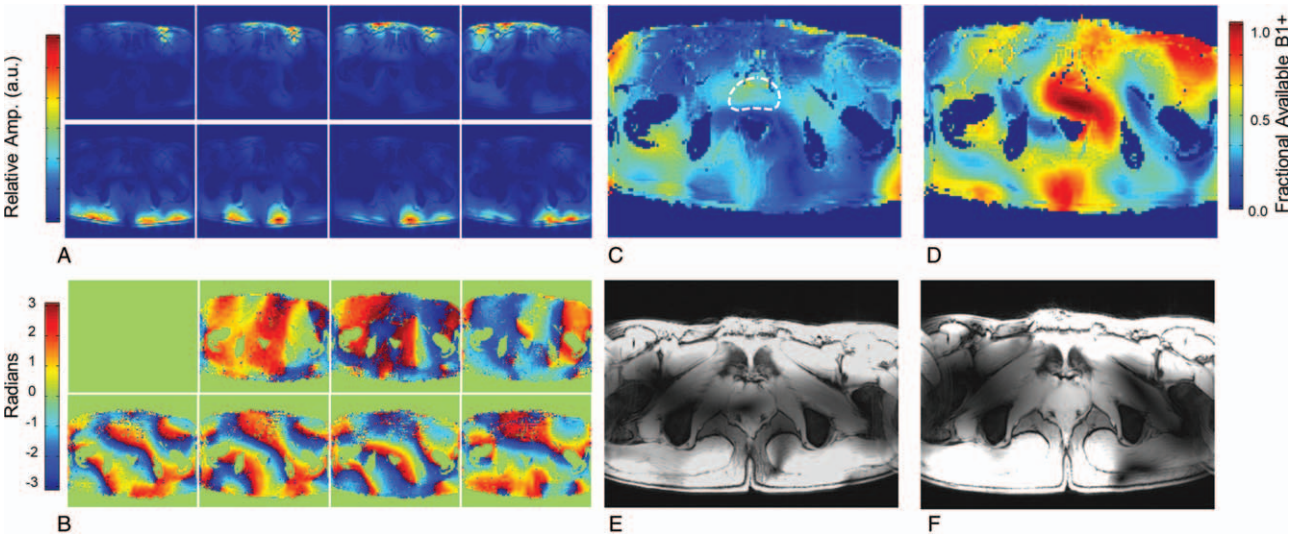

FIGURE 2. Magnitude (A) and relative phase images (B) acquired by transmitting through a single channel and receiving on all channels of an 8-element transceiver array. The magnitude images are created by the sum of magnitude images from each receive channel. The relative transmit phase for element 1 shows zero phase throughout, as this element is arbitrarily chosen as the reference channel. Theoretical fraction of available B_1^+ given (C) before and (D) after RF shimming using a phase-only optimized for efficiency in the indicated ROI (dashed white curve). Gradient echo images acquire (E) before and (F) after RF shimming. Adapted with permission of John Wiley and Sons from Metzger GJ, Snyder C, Akgun C, et al. "Local B1+ shimming for prostate imaging with transceiver arrays at 7T based on subject-dependent transmit phase measurements." *Magnetic Resonance in Medicine*. 2008;*59*(2):396-409; permission conveyed through Copyright Clearance Center, Inc.

potential benefit of reducing peak local SAR, as shown in EM simulations; the peak local hot spot relocates anatomically with each solution thus benefitting from the time averaging process used to monitor power deposition (Fig. 4).

When the goal is an image with homogeneous contrast or B_1^+ over larger FOVs, the time interleaved acquisition of modes (TIAMO) technique is highly effective (Fig. 5). This technique provides improved signal homogeneity without the need for subject-specific RF shimming, by utilizing 2 complementary RF shims interleaved during the acquisition such as circularly polarized (CP^+) and CP^{2+} modes.[73] Reconstruction of the combined data uses the idea of virtual coils in a parallel imaging reconstruction pipeline enabling higher accelerations, which partially compensates for the increased acquisition times required. For larger FOVs, this technique has been shown to provide better B_1^+ homogeneity than a single static RF shimming solution, is relatively SAR efficient while producing the desired contrasts including T2 weighting,[74] and has the possibility of being implemented on single transmit systems.[75]

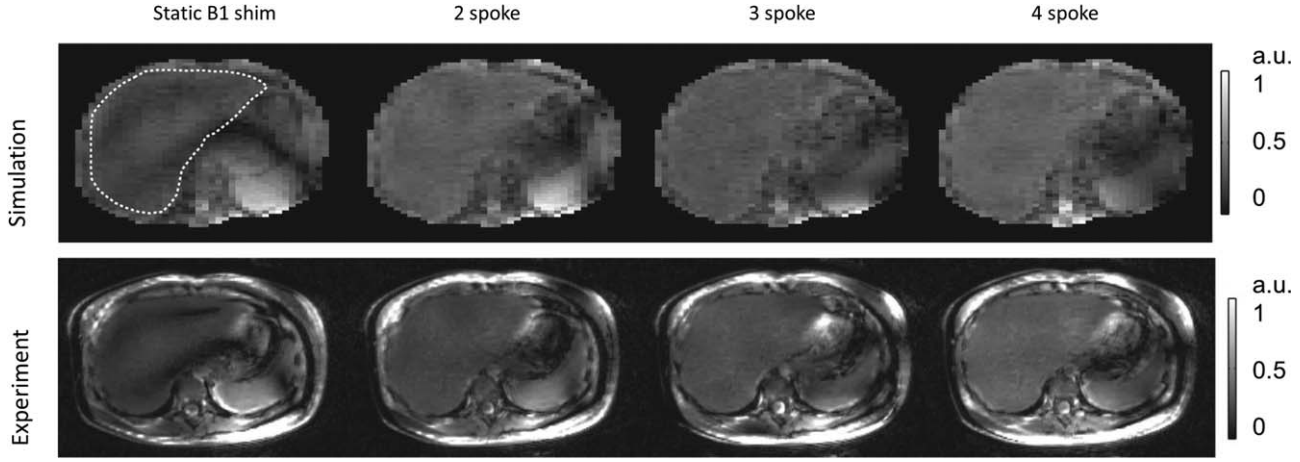

FIGURE 3. Comparison of static RF shimming and multispoke pTX pulse design when used to mitigate B_1^+ inhomogeneity in liver MRI at 7T. (Upper row) Bloch simulations of the transverse magnetization for various solutions using static and dynamic RF shimming. The dashed outline indicates the region over which the flip angle was homogenized. (Lower row) Experimental results from implementing the static and dynamic solutions demonstrating the improved ability of dynamic RF shimming to produce homogeneous results. Images Courtesy of Dr Xiaoping Wu, University of Minnesota, MN.

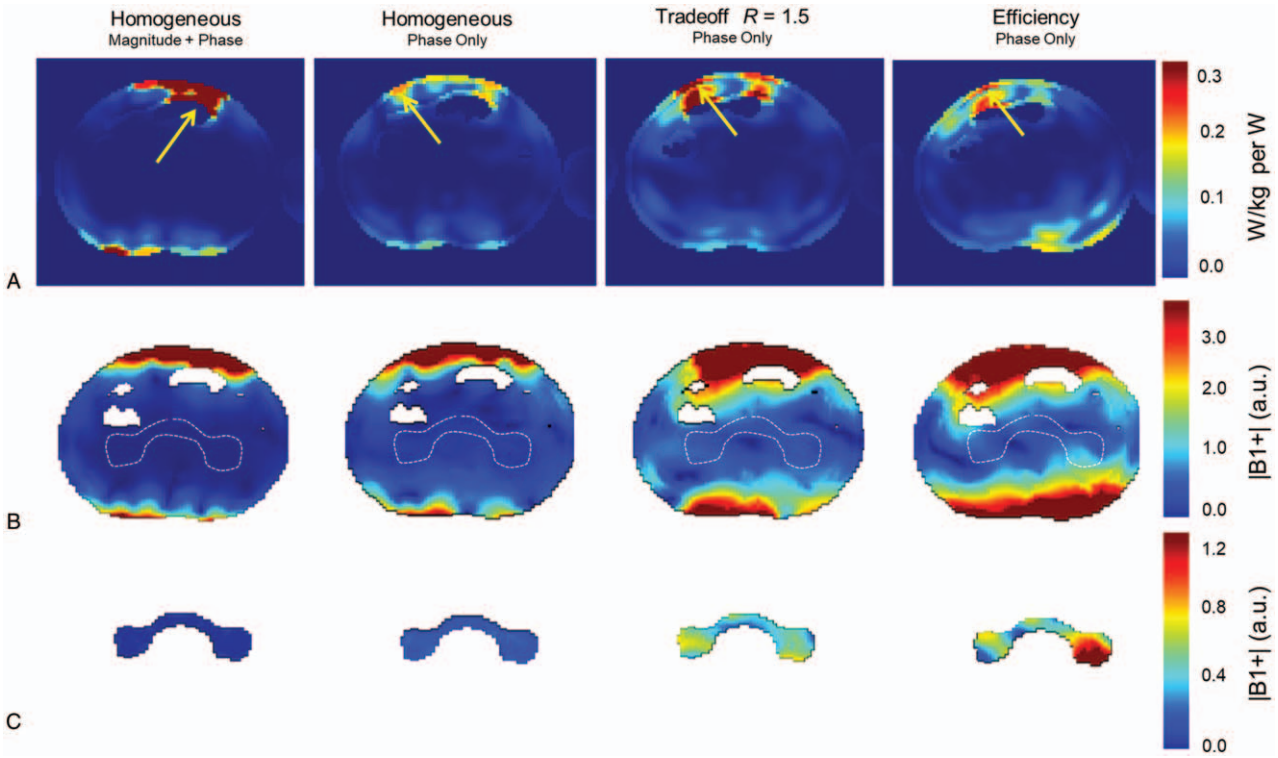

FIGURE 4. Axial slices from simulation at the level of the peak local SAR for 4 different B_1^+ shim solutions of the kidney (A). Predicted B_1^+ distributions with the same RF shim solutions at the level of the kidneys with the anatomical shim target shown (B, broken white curve). The B_1^+ distributions from the region of the RF shimming target (C). Republished with permission of John Wiley and Sons from Metzger GJ, Snyder C, Akgun C, et al. ''Local B_1^+ shimming for prostate imaging with transceiver arrays at 7T based on subject-dependent transmit phase measurements.'' *Magnetic Resonance in Medicine.* 2008;*59*(2):396-409; permission conveyed through Copyright Clearance Center, Inc.

Another promising approach is to embrace the RF field nonuniformity by imaging with freely varying heterogeneous RF fields and employing a dictionary-based image reconstruction algorithm.[76] This so-called plug-and-play MR fingerprinting (PnP-MRF) approach relies on two or more dynamically changing RF excitation patterns to generate sufficient B_1^+ in all parts of the imaging FOV. In reconstruction, tissue relaxation parameters and B_1^+ fields are simultaneously estimated using a dictionary-based approach.

EXOGENOUS CONTRAST AGENTS

Gadiolinium (Gd) based chelates are the most common exogenous contrast agents used in a wide range of MRI applications. Other than perfusion applications using dynamic susceptibility contrast, it is primarily the T1 shortening aspect of the Gd-based contrast agents, which is used with T1-weighted (T1w) imaging. However, as the static magnetic field increases, R1 relaxivity remains relatively stable while $R2^*$ relaxivity increases rapidly and nonlinearly with concentration in biological tissues becoming large enough where it no longer can be ignored. [77,78] (Fig. 6A). This nonlinear effect is observed in the body, both blood and tissue, as the gadolinium is compartmentalized leading to a field strength dependent susceptibility effect that is not observed in aqueous solution.

For some applications, the increase of native T1s in tissue provides advantages for noncontrast studies including angiography and arterial spin labeled perfusion. The interest in performing noncontrast vascular and perfusion imaging has increased, as the evidence has been presented showing Gadolinium toxicity.[79–82] While the risk of complications increase with less stable linear compounds, when repeated and/or double doses are given and when subjects present with renal insufficiency, the potential to provide equivalent clinical information without contrast is desirable. Several studies have shown that with the appropriate RF coils, management strategies, and acquisition methods, improved angiography[83–85] and perfusion results can be achieved in the brain at 7T compared with 3T. Meanwhile, target-specific applications are detailed for the torso in the sections below.

The increased susceptibility effect of exogenous contrast agents can also be an advantage. For example, a dextran coated ultra-small superparamagnetic iron oxide particle was reintroduced for evaluating the spread of prostate cancer to the lymph nodes. By infusing 24 to 36 hours before imaging, these particles are taken up by macrophages and cause darkening of healthy lymph nodes while nodes with progressive metastatic disease stay bright.[86] By using water and fat selective imaging and TIAMO to mitigate field inhomogeneities, high-resolution images of the abdomen and lymph nodes are possible, taking advantage of increased signal to noise of the background tissue and increased susceptibility contrast of the nanoparticle laden lymph nodes[87] (Fig. 5).

SAFETY

Local SAR

The primary safety concern for UHF body imaging is local heating. The common approach adopted by different institutions is to validate EM models of the RF coil via B_1^+ mapping, measurement of the scattering parameter matrix, and temperature measurements to assess local SAR. Then, peak local 10 g averaged SAR in one or more human body models is determined using the validated RF coil model with a variety of shim settings.[39,44–46,48] Finally, worst-case SAR levels or conservative SAR scaling factors are applied to determine

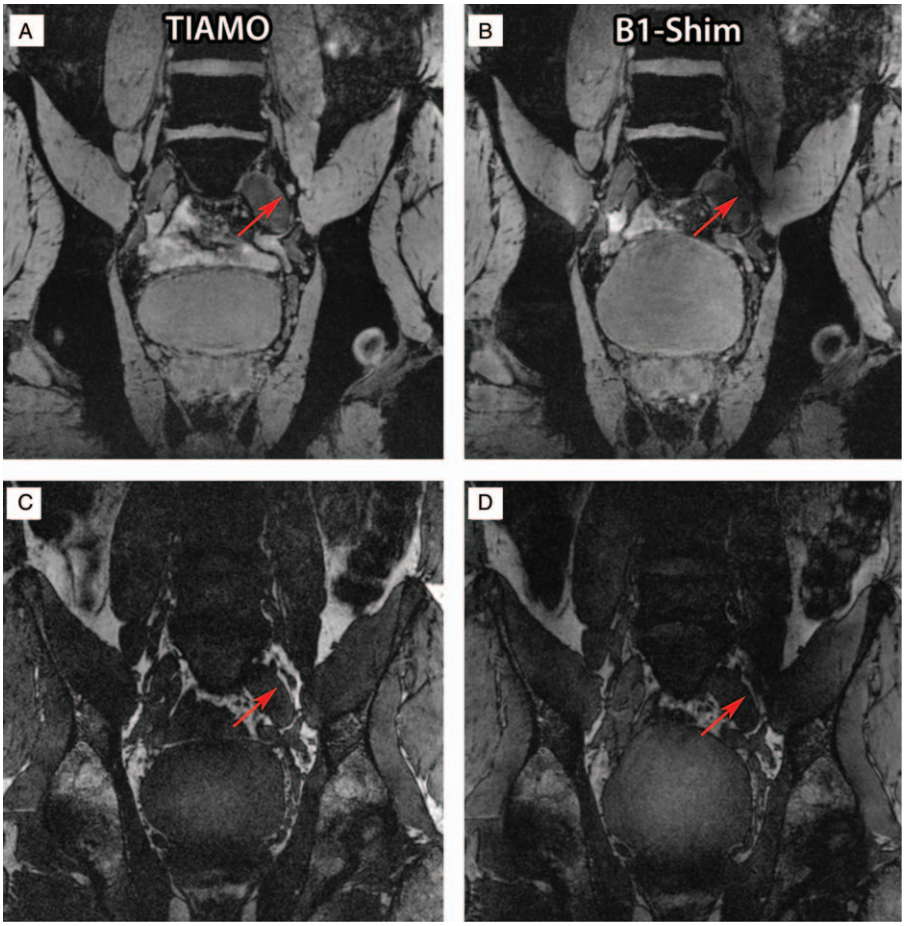

FIGURE 5. Water (A and B) and lipid selective (C and D) images of a volunteer's lymph node (red arrows) close to the left iliac vein acquired using the TIAMO method (A and C) and static phase-only B_1^+ shimming (B and D). Because of the B_1^+ inhomogeneity, the lymph node is not visible in the static phase-only B_1^+ shimming approach. Republished with permission of John Wiley and Sons from ''High resolution MR imaging of pelvic lymph nodes at 7 Tesla.'' *Magnetic Resonance in Medicine*, Philips BWJ, Fortuin AS, Orzada S, Scheenen TWJ, Maas MC. 2017;*78*(3):1020–8.

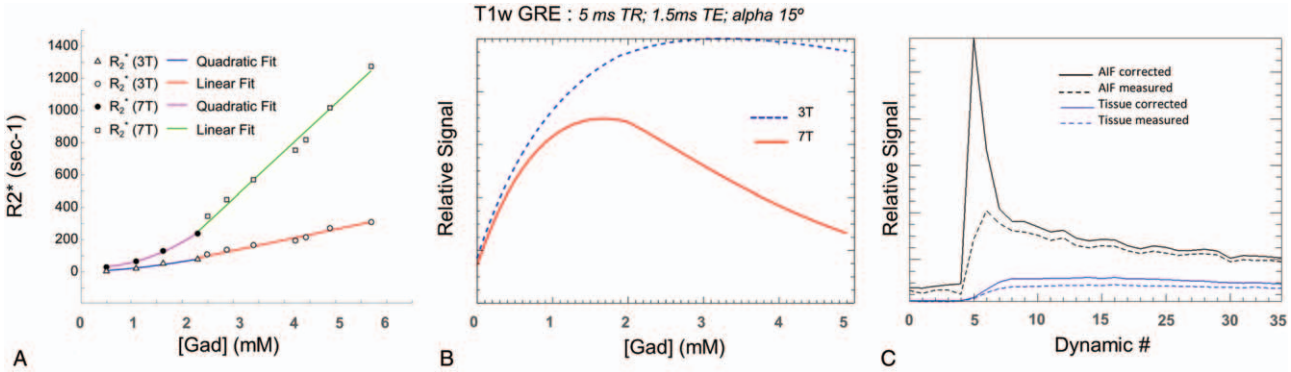

FIGURE 6. Although the r1 relaxivity for gadolinium contrast agents increases from 3T to 7T (3.2 mM/s for Magnivist), the r2* relaxivity increases dramatically when compartmentalized as in blood and tissue. Nonlinear r2* relaxivity in oxygenated human blood at 3T and 7T (A). At concentrations above 2 mM, a linear relationship relaxivity is observed (68.9 mM/s at 3T and 290.8 mM/s at 7T. Signal characteristics of a T1w GRE sequence (B) with increasing Gd concentration showing rapid signal loss at7T with higher concentrations. Arterial input function and tissue signal intensity curves from a DCE-MRI prostate study (C). Acquired with a multiple-echo acquisition allowed for correction of time intensity curves at the expense of temporal resolution.

channel-specific power limits used for human imaging. Intersubject variations in body size, shape, and composition can lead to significant differences in simulated SAR in generic body models versus actual SAR in the subject. Alon et al[88] demonstrated that B_1^+ distributions in different samples can be well correlated while significant differences in SAR and temperature rise can occur, therefore solely relying on B_1^+ distributions for coil model validation might lead to errors. Creation of individualized EM models, improvements in real-time power monitoring, and advances in thermal modeling with in vivo validation have the potential to improve the reliability and accuracy of safety evaluations.[67,89–98]

PROSTATE

Multiparametric MRI of the prostate is playing an increasingly important role in the management of prostate cancer. The core imaging contrasts used in the standard interpretation of prostate MRI as defined by the Prostate Imaging Reporting and Data System (PI-RADS) include T2-weighed anatomic imaging (T2w), diffusion-weighted imaging (DWI), and dynamic contrast enhanced MRI (DCE-MRI).[99] However, despite recent advances, the continued development of prostate imaging methods is driven by the desire to noninvasively differentiate men with aggressive disease from indolent disease. Faced with uncertainty, many men with a diagnosis of prostate cancer choose unnecessary treatment at a great cost to the health care system while causing men to suffer from associated comorbidities. The development of acquisition methods and hardware to realize the advantages of UHF drive developments in this area in the hopes of improving disease management.[100]

Target-specific Shimming

The prostate is a relatively small organ with a location in the male pelvis slightly anterior to the midline of the body. As a result of its position and the image contrasts relevant for diagnosis, the peak B_1^+ and peak local SAR are the primary design criteria for RF shimming. First studies in the prostate at 7T using an 8-channel stripline array demonstrated that subject-specific phase-only RF shimming can increase the average B_1^+ and decrease the percent inhomogeneity by over 4-fold[59] (Fig. 2C–F). While simulations demonstrate a higher local SAR for an equal input power after RF shimming, the possibility of using 16 times less power to achieve the same average B_1^+ more than compensates by greatly increasing the SAR efficiency ($B_1^+/\mathrm{SAR}^{0.5}$). Therefore, while the primary benefit of local B_1^+ shimming in the prostate through transmit phase optimization is an increase in transmit efficiency, homogeneity and SAR efficiency also improve. It must be emphasized that, in the absence of RF shimming, performing the desired imaging studies on the initial 7T system, which were driven by single 8 kW RF amplifiers, would not have been possible. Although these initial studies were promising, limitations remained. Limited peak B_1^+ reduced the ability to image larger subjects, while poor SAR efficiency reduced the number of slices obtainable when acquiring T2w anatomic images. An alternative strategy to address the limitations of T2w imaging in the prostate at 7T was demonstrated by Maas et al,[101] where they prolonged RF pulses and used VERSE to reduce the peak power and SAR with the possibility of increased blurring due to the prolonged echo spacing of the refocusing pulses. Other strategies required progress on the hardware front. Further developments in RF coils paralleled the development of pTx systems and acquisition strategies to help overcome the limitations.

Body RF Coils

Most of the external RF arrays for imaging the prostate are well suited for imaging other anatomies in the torso. However, the prostate is an ideal target to evaluate coil performance because of its relatively small size and central location, which requires only the most basic RF shimming methods. In addition, it is impacted less from physiologic motion compared with other organs in the torso, which allows quantitative B_1^+ mapping to be performed. Therefore, using the prostate as the anatomical target, several general torso imaging arrays are presented in this section.

A 16-channel stripline array was developed[54] and used on a pTx-v1 system with sixteen 1 kW transmit channels[39] (Fig. 7A). Compared with an 8-channel version of the coil, the increased element count and density increased the transmit and receive performance by 22% along with improved parallel imaging performance, providing sufficient transmit and SAR efficiency to perform many of the acquisitions required in a clinical examination. However, increased element density came at the expense of complexity including the need for decoupling capacitors on both the conductor and ground planes due to the close element spacing. Usability of this array was somewhat limited due to its weight, rigid structure, and the necessity to manually tune and match the elements on each subject.

An 8-channel array comprising a center-fed microstripline resonator with meanders was introduced by Orzada et al.[37] The use of air as a dielectric rather than a polytetrafluoroethylene (PTFE) block greatly reduced the weight of each element. Using this array, a multireader study looking at anatomic T2w image quality in patients reported ''satisfactory'' to ''good'' ratings for image quality and in the identification of anatomic structures. In 17 patients, pathologically confirmed prostate cancer was identified on pre-surgical T2w TSE imaging including 20 slices acquired in ~2 minutes with a resolution of $0.75 \times 0.75 \times 3\,\mathrm{mm}^3$.[102] This coil was also used in the work presented in Fig. 5 and has the advantage of not requiring subject-specific tuning and matching.

Dipole antenna arrays were introduced by Raaijmakers et al[38] for prostate imaging. Subsequently, meanders were added to improve SAR efficiency by 50% without compromising B_1^+ efficiency. The average B_1^+ in prostates between 12 and18 μT was obtained for volunteers imaged on pTx-v1 systems with 8x2 kW amplifiers[45] (Fig. 7B). In general, dipole antenna elements have favorable characteristics for body imaging such as improved B_1^+ efficiency at greater depths and more uniform transmit-receive profiles compared with striplines or loops.[103] Practical advantage of the fractionated dipole array compared with the original stripline elements and similar to the meander striplines are the flexible housing and its lower Q thus obviating the need for subject-specific tuning and matching to maintain acceptable performance. An 8-channel fractionated dipole transceiver array with an integrated 16-channel loop receiver demonstrated a 1.7 to 2.8-fold increase in SNR compared with the same individuals observed on a 3T with a commercial body array coil.[43,104] Along with increased SNR, lesion contrast to noise also increased in the patients studied.

On receive, geometrically decoupled loops and dipoles have been shown to increase the SNR in the head[105,106] and later in the prostate.[104] On transmit, the benefits of the combination have been explored with a 16-channel combined loop-dipole transceiver array (16LD)[46] (Fig. 7C). Experimental results demonstrated that the 16LD had more than 20% higher SNR and B_1^+ transmit efficiency than both the previously detailed 16-channel stripline and a 10-channel version of the fractionated dipole array.[107] The 16LD is a preferable way of increasing channel count and element density as compared to the earlier 16-channel stripline array. The loops and dipoles of the 16LD are geometrically decoupled eliminating the need for active decoupling. In addition, the performance of the 16LD performed well at multiple locations and on subjects with various sizes without the need for subject-dependent tuning and matching just as with the microstripline with meanders[37] and the fractionated dipole.[45] Maintaining this characteristic as a plug-n-play coil is critical for clinical applications.

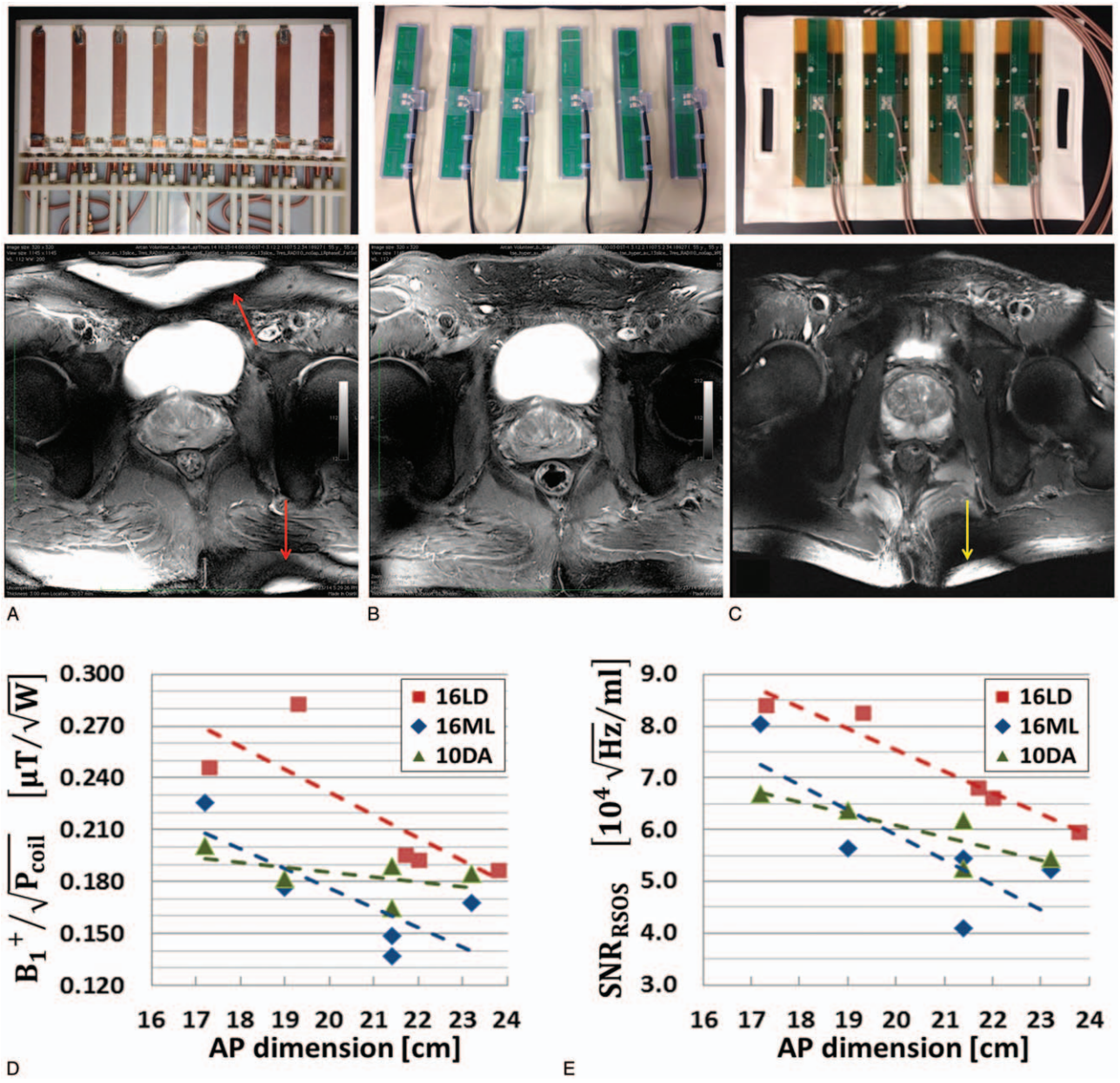

FIGURE 7. Body array comparison with representative T2w TSE anatomic images. A 16-channel micro-stripline (16ML) with 8 anterior and 8 posterior and capacitive decoupling between adjacent ground planes and conductors (A). Rods attached to variable capacitors are seen for subject-specific tuning and matching. Ten-channel fractionated dipole antenna (10DA) array with 6 anterior and 4 posterior elements (B). Sixteen-channel loop-dipole array with 8 fractionated dipoles and centrally geometrically decoupled loops (C). All coils had similar circumferential coverage with their relative spacing to the nearest neighbor dictated by design. The relative performance of these 3 arrays with respect to (D) transmit efficiency and (E) SNR in the target anatomy of the prostate are shown versus men with increasing size. The combination of loop dipole-coil presented with improved SNR and transmit efficiency. The uniform cross-sectional images produced by 10DA highlight the benefits of this resonant structure for body imaging in general. While overflipping is more pronounced with the 16LD due to the inclusion of loop elements on transmit (yellow arrow), the characteristically high B_1^+ gradient is more prevalent with the 16ML (red arrows).

Endorectal Coils

The development of prostate imaging at 7T has followed a similar path as lower field strengths involving both surface arrays and endorectal coils (ERCs). The ERC needs to be a transceiver if used without a body transmit coil. Initial safety testing of a transceiver ERC was validated with EM simulations, electric field probe measurements, and thermometry to ensure that surface temperatures did not exceed safety guidelines.[108] Although performing imaging with a transceiver ERC is difficult because of the intense B_1^+ inhomogeneity, it has been demonstrated quite useful in spectroscopy

acquisitions where the high peak B_1^+ generated with excellent SAR efficiency can be used along with adiabatic localization strategies.

Due to the inhomogeneity on transmit and the desire to optimize SNR, the ERC was also investigated in comparison to and in combination with an external surface array as a receive-only coil.[54] A study using a similar receive-only balloon-type ERC for reception was used with the 8-channel meander external array for transmit. This configuration demonstrated the performance of a multiparametric MRI protocol including anatomic T2W, DWI, and spectroscopy in 14 patients with biopsy-proven prostate cancer.[109] High-resolution anatomic imaging was achieved with $0.3 \times 0.3 \times 2\,mm^3$ resolutions in 2:59 for 29 slices. Multishot diffusion was acquired with the highest resolution of $1.4 \times 1.4 \times 2\,mm^3$ in a scan time of 4:22 for 22 slices. It was concluded that high-resolution anatomic imaging and acceptable DWI could be acquired in clinically acceptable acquisition times; however, the robustness of the techniques needed to be improved.

Multichannel ERCs have also been evaluated with improved management of B_1^+ and increase receive sensitivity. A balloon-type coil, which pairs a loop with a strip-line element[110] and a 2-loop design in a solid, sterilizable reusable housing, provided more than 4-fold SNR gain in the prostate.[111] Imaging results using the multichannel ERC with an external transmitter were possible by incorporating detuning circuitry.[112] By transmitting with a 16-channel loop-dipole array and combining with the 2-channel solid ERC, high-quality anatomic and functional imaging data were obtained (Fig. 8).

Spectroscopy in the Prostate

Three primary strategies have been used for performing proton spectroscopic imaging in the prostate. The initial ^1H spectroscopic imaging studies in the prostate at 7T made use of the increased transmit B_1^+ field of a transceiver ERC.[113]

A semi-LASER sequence provided spatial localization with a chemically shift selective refocusing pulses optimized for water a lipid suppression, also referred to as MEGA.[114] High-quality spectra were obtained with echo times of 56 ms and a repetition time of 2 seconds. The B_1^+ sensitive slice selection RF pulses of semi-LASER was run parallel to the ERC, while a pairs of adiabatic pulses provided high bandwidth refocusing minimizing both the effects of the inhomogeneous B_1^+ and of chemical shift artifacts. The inter-pulse timing of the sequence was later modified to accommodate more selective MEGA pulses for improved decoupling of the 1.8 and 2.1 ppm protons of the polyamines while also providing an absorptive citrate spectrum.[115]

Subsequent studies with the 2-channel balloon-type ERC introduced above enabled full adiabatic localization due to improved SAR efficiency.[110] The coil could generate a B_1^+ of at least 20 mT at a depth of 3.5 cm into the prostate where the duty cycle could be increased 4-fold compared with an ERC with a single loop.

When using the surface array for transmit, the semi-LASER sequence was found to exceed SAR limits. Therefore, a double-spin echo sequence with optimized spatial-spectral refocusing pulses was designed. This sequence, which no longer employed adiabatic pulses due to a relatively homogeneous B_1^+or the surface transmitter, allowed ^1H spectroscopic imaging to be performed in the prostate

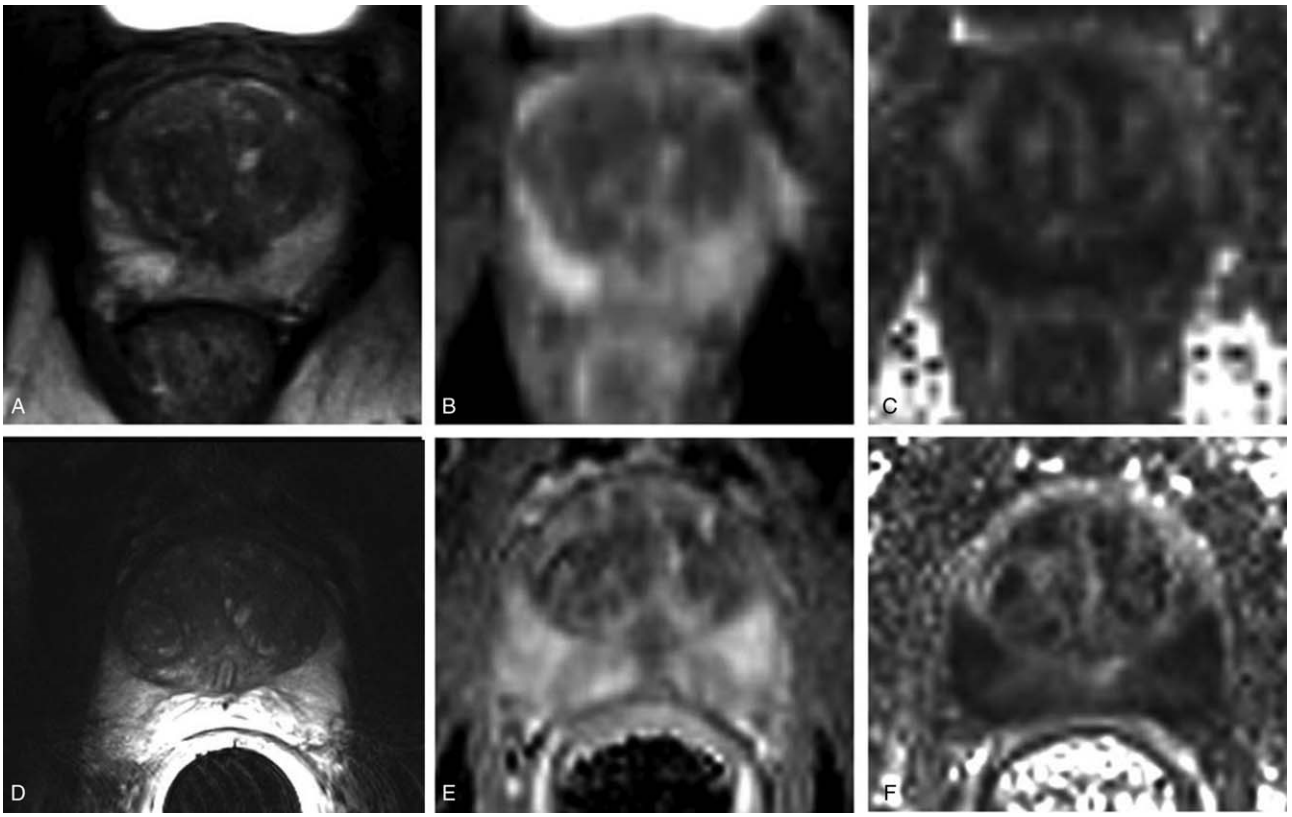

FIGURE 8. T2-weighted anatomical images (A,D), apparent diffusion coefficient (ADC) (B,E), and fractional anisotropy (FA) maps (C,F) of the prostate. Images in the top row (A–C) and bottom row (D–F) were acquired using 16LD alone and in combination with a 2-channel ERC, respectively. Republished with permission of John Wiley and Sons from ''Development and evaluation of a multichannel endorectal RF coil for prostate MRI at 7T in combination with an external surface array,'' Erturk MA, Tian J, Van de Moortele PF, et al. *JMRI*. 2016;*43*(6); permission conveyed through Copyright Clearance Center, Inc.

with an 8-channel external array on transmit using a receive-only ERC for reception.[37,116]

The improved quantification of metabolites due to increased spectral dispersion and SNR observed in the brain is also relevant for studies in the torso.[5] To investigate the benefits in prostate spectroscopy, simulated and acquired data were evaluated by fitting with LC-Model. Data were acquired with a 16-channel stripline transceiver array combined with a single-channel balloon-type ERC on receive. It was demonstrated that improved delineation between overlapping metabolites is possible at higher fields as indicated by improved Cramer-Rao lower bounds (CRLB) and reduced correlation coefficients (CCs) between peaks[6] (Fig. 9). The increased spectral dispersion, especially for choline and creatine which overlap with the strongly coupled spermine signal, greatly benefit from quantification at increased field strength. The ability to individually quantify these metabolites may prove clinically relevant. For example, HRMAS data from Swanson et al[117] demonstrate that the polyamine resonance was the most correlated with cancer aggressiveness. Maintaining spectral quality is imperative to realizing the benefits in spectral quantification. Field probes have been presented as a means to maintain spectral fidelity in the presence of B_0 field variations. Arteaga de Castro et al[20] demonstrated the use of field probes for spectroscopy in the prostate.

Contrast Studies in the Prostate

Dynamic contrast enhanced imaging is one of the 3 main imaging methods used in PI-RADS. To date, only a few studies have investigated the performance of DCE-MRI in the prostate at 7T. A typical acquisition requires a bolus injection of contrast followed by a time-resolved 3D GRE acquisition where volumes are acquired as rapidly as possible. A tradeoff of resolution for speed provides higher temporal resolution providing for improved assessment of first pass kinetics and pharmacokinetic modeling. The bolus injection of contrast results in short-lived but high concentrations of Gadolinium in the blood resulting in $T2^*$ values approaching 1 ms. Measuring the arterial input function in such cases becomes impossible unless the $T2^*$ can be corrected[118] (Fig. 6B,C). While the impact is greatest in the vessels where Gadolinium concentrations are the highest, $T2^*$ signal loss in tissue should be accounted for to avoid the underestimation of pharmacokinetic parameters.[118] Alternatively, imaging acquisitions using ultra-short echo times can effectively minimize the effect of $T2^*$ shortening.[119,120]

CARDIOVASCULAR

Overview

MRI of the cardiovascular system has proven to be a powerful noninvasive tool providing a wealth of information for the assessment of structure and function, blood flow, tissue perfusion, and viability. The previously mentioned challenges of UHF imaging in the torso are compounded in the heart because of cardiac and respiratory motion. While the potential advantages of UHF-MRI in cardiovascular imaging have been expertly detailed in previous reviews,[27–29,121] this section will focus primarily on detailing the evolution of specific critical technologies, hardware, and acquisition methods necessary to achieve the promised advantages of UHF in this anatomy focusing on functional imaging, coronary magnetic resonance angiography, and 4D-flow

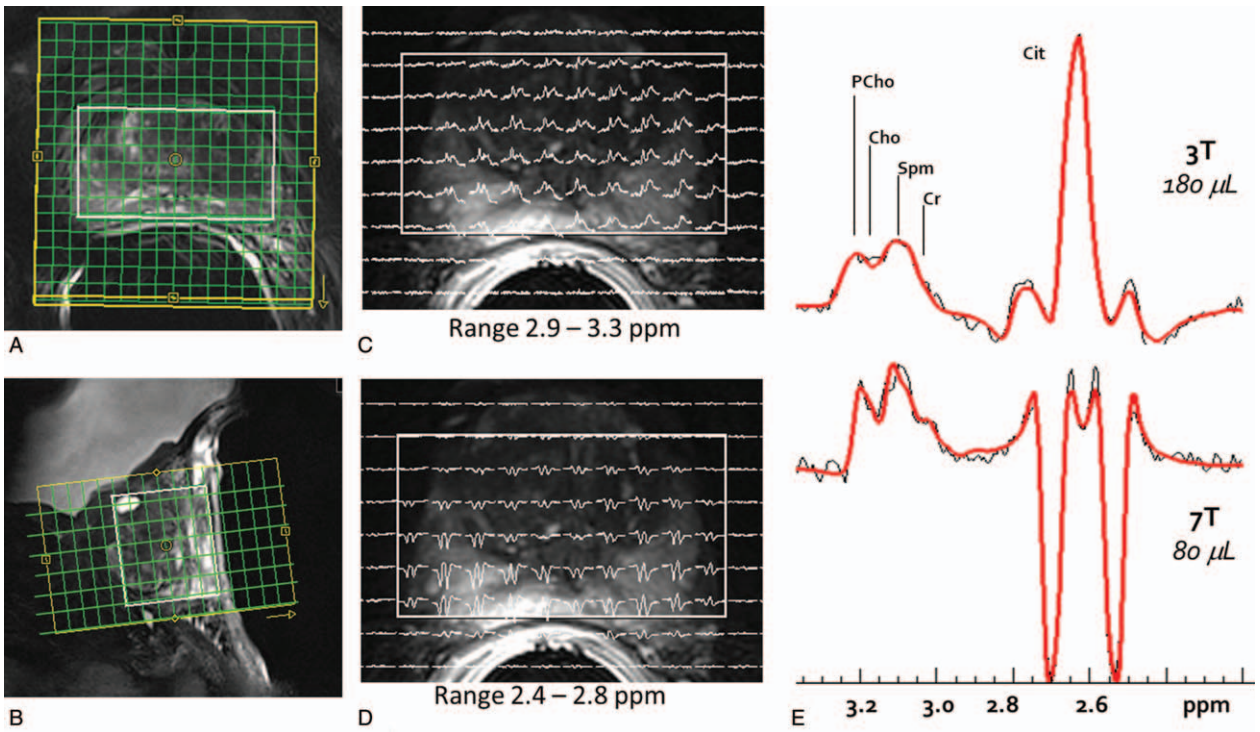

FIGURE 9. (A, B) Planning of the 3D spectroscopic imaging acquisition with the FOV (yellow box), the semi-laser localized volume (white box), and the acquired phase encoded acquisition grid (green). A grid of spectra from slice 4 of the 8-slice acquisition (right). (C), The ppm range of 3.3–2.9 includes the choline signals (PCho & Cho), polyamines (primarily spermine – Spm), and creatine (Cr) resonances, while (D) the 2.8–2.4 ppm range covers the citrate (Cit) multiplet. E, The LCmodel-based fitting of 3T and 7T spectra from the same individual was used to assess the Cramer-Rao lower bound (CRLB) and correlation coefficients (CC). Consistently lower CRLB for all metabolites and CC between Spm and the overlapping peaks of tCho and Cre demonstrate that quantification is improved for the prostate metabolites across the entire depth of prostate at 7T.

studies. Other clinically relevant acquisitions that have been adapted for UHF but will not be further covered include T1 measurements in the presence of incomplete inversion,[122] tailored shimming and acquisition techniques for $T2^*$ mapping,[123,124] and first-pass myocardical perfusion imaging using improved saturation-based methods.[125]

Physiologic Motion

For many cardiovascular applications, there is a need to measure data over several cardiac and respiratory cycles requiring accurate triggering or gating during data acquisition. The primary feature in the cardiac heartbeat used for cardiac triggering is the R-wave as determined by an electrocardiographic (ECG) recording of the heart beat through multiple leads placed on the chest wall. The challenges of using ECG in MRI are the potential for heating of the electrodes, gradient-induced noise in the leads, and the MHD effect, which generates Hall Effect voltages as a result of blood, a conductive fluid, passing through a magnetic field.[126] The MHD effect and other artifacts in the ECG trace reduce the ability to reliably identify the R-wave even when using a vector ECG (VCG), which includes associated algorithms for processing multidimensional traces.[127,128]

Alternative strategies of triggering have been developed that avoid the artifacts present in a typical VCG. The first is the acoustic cardiac trigger (ACT), which uses a phonocardiograph for detecting the onset of the first heart tone.[129] This method uses an MR-compatible stethoscope, is not influenced by the MHD effect, and is free from artifacts due to the EM fields. It was demonstrated that the ACT had favorable characteristics compared with ECG, as it had less jitter in R-wave determination but it had increased latency of 35 ms.[130] While shown to be robust for prospective triggering and retrospective gating, the latency may be detrimental for some applications.

Several methods have also been proposed for gating without the need for additional hardware to be placed on the subject. The first it the pilot tone (PT) approach originally presented for respiratory gating[131] and then for cardiac gating[132] applications. The PT uses a signal generator to produce small amplitude PT signal outside the frequency band of the MR signal but inside the received frequency band. Modulation of the PT signal is used to characterize respiratory and cardiac motion. Another approach requires no additional hardware and involves the evaluation of the RF scattering of a parallel transmit coil to track diaphragm position[133] or cardiac phase.[134] For cardiac acquisitions, the VCG and ACT allow for prospective triggering of sequences, while these alternative methods are appropriate for gating, which could be used as an alternative for self-gating when non-radial acquisitions are desired.

Target-Specific Shimming

Although initial 7T cardiac studies of the heart used anteriorly placed quadrature loop coils, it has been shown that multichannel transceiver arrays are necessary to explore the full potential of UHF. Depending on the RF coils and transmit hardware available, different B_1^+ management strategies have been employed to effectively use these multiple-channel arrays. The methods that worked effectively in the prostate, most typically an efficiency phase shim, are not sufficient in the heart, as it is a much larger organ and is more asymmetrically positioned in the body. Although many cardiac studies have used static RF shimming solutions optimized to obtain a homogeneous B_1^+ from either EM simulations[135] or subject-specific calibration,[136] dynamic RF shimming has demonstrated improved homogeneity while decreasing overall RF energy deposition.[66] By obtaining rapid calibration data using the low flip angle approximation approach for B_1^+ [62,137] and rapid B_0 maps with cardiac triggering and breath-holding, Schmitter et al[66] compared a 2-spoke RF pulse against a static RF shim (ie, 1-spoke solution). For a given field nonuniformity (coefficient of variation, CV), the 2-spoke solution provided a reduction of total RF energy by over 50% averaged over multiple imaging orientations. To create a more robust solution less sensitive to respiration effects, calibration data were acquired at multiple respiratory positions and used as virtual slices for pulse optimization.[21] Further extending these methods, multispoke pTx dynamic RF shimming was combined with simultaneous multislice (SMS) methods demonstrating it as a viable approach to uniformly acquiring and accelerating the acquisition of functional cardiac data at UHF.[65]

Functional Cardiac Applications

A staple in the cardiac MR (CMR) evaluation of heart function involves CINE imaging where the highly choreographed contraction of the heart's chambers is captured in multiple frames across the cardiac cycle. The segmented data acquired across several heart beats require accurate timing either through prospective triggering or retrospective gating using one of the triggering/gating methods mentioned above. High contrast is desired between the myocardium and the blood pool allowing important metrics to be easily calculated such as the cardiac output and ejection fraction. Although there is high satisfaction with balanced steady-state free precession (SSFP) acquisitions to provide this contrast at 1.5T, the ability to acquired CINEs was a necessary entry point for UHF CMR explorations, which typically can involve the assessment of function, perfusion, and tissue viability. CINE acquisitions are often used to evaluate the performance of UHF RF coils for cardiac imaging with the metric of success being the ability to obtain higher resolution data more rapidly in fewer breath holds or during free breathing.

Before further advancing the field, comparisons between 1.5T and 3.0T were made against 7T with respect to standard diagnostic metrics derived from functional imaging studies. It was shown in multiple reports that the stroke volumes, cardiac mass, and multiple other parameters were similar at all field strengths in the left ventricle[65,136,138–140] and right ventricle[140] opening the doors to pursue other studies in the heart. Each successive study added more complex hardware including RF coils and transmit chain architectures, but the results were similar. One conclusion based on the later studies was that the contrast achievable at 1.5T with a SSFP acquisition was obtainable with a T1w GRE at 7T.[136,139] Although it was demonstrated that an SSFP can be acquired at 7T, it was difficult to implement within SAR constraints[136] (Fig. 10).

A later study investigating patients with hypertrophic cardiomyopathy (HCM) demonstrated subtle morphological details on CINE imaging at 7T, which correlated with regions of extended hypertrophy and fibrosis identified on late gadolinium enhancement studies performed at 3T.[141]

Cardiac-Specific RF Coils

Although some of the cardiac imaging evaluations have been successfully performed with relatively simple RF coils, imaging studies seeking increased parallel imaging performance, improved management of B_1^+, and increased SNR and contrast homogeneity have developed and deployed RF arrays with increasing numbers of channels.[34,40,41,44,49,142–144] Depictions of these arrays and results obtained from them are provided (Fig. 11).

A series of transceiver loop arrays with 4, 8, and 16 elements, with adjacent loops sharing a common conductor, were constructed and compared for UHF CMR.[40,143] The 16-channel array was the only iteration with elements distributed along the foot-head dimension and consisted of 2×4 elements both anterior and posterior. These configurations were evaluated using a single 8 kW RF amplifier driven through a splitter where RF phase shimming was employed based on calculations determined from EM simulations.[135] The 16-channel array had the highest image quality ratings and best parallel imaging performance, while both the 8-channel and 16-channel arrays were reported to produce diagnostic quality images.

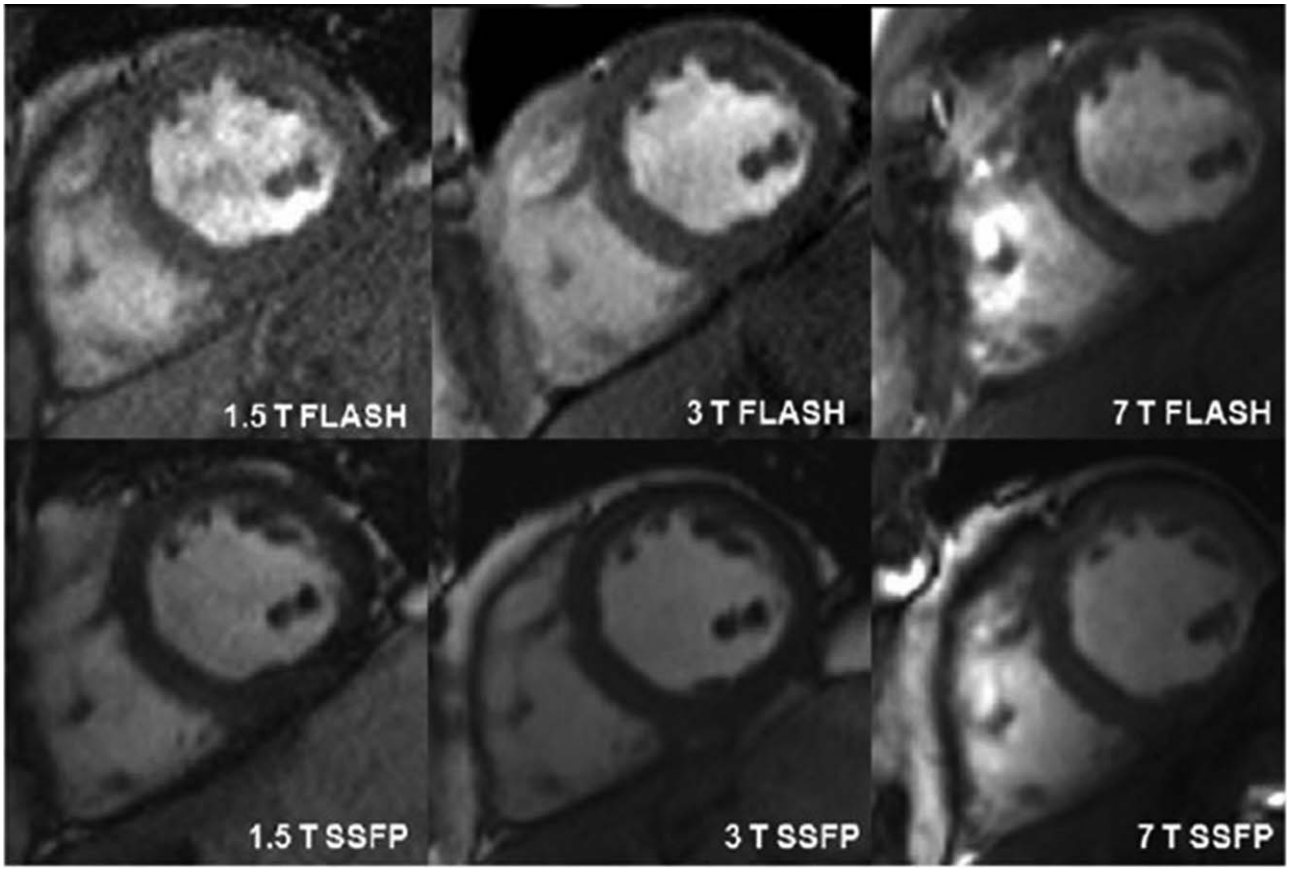

FIGURE 10. Short axis cardiac images acquired at 1.5, 3, and 7 T using fast low angle shot (FLASH) and steady state free precession (SSFP) sequences in the same subject. Republished with permission of John Wiley and Sons, from ''7 Tesla (T) human cardiovascular magnetic resonance imaging using FLASH and SSFP to assess cardiac function: validation against 1.5 T and 3 T,'' Suttie JJ, Delabarre L, Pitcher A, et al. *NMR in Biomedicine*. 2012;*25*(1).

Increased functionality was proposed in the form of a 32-channel modular coil array comprised of 8 independent building blocks conforming to the chest wall, with each block containing 4 transceiver loop elements (Fig. 11A).[41] An EM simulation based phase shimming optimizing homogeneity was applied which decreased transmit efficiency to 30% of that obtained with a CP-like mode. Along with supporting a 1-dimensional parallel imaging reduction factor of 4, cine imaging with $1.1 \times 1.1 \times 2.5\ mm^3$ is 6-fold better than standard cine protocols at 1.5T.

A 16-channel bow tie dipole antenna array arranged in 2 rows was shown to improve parallel imaging performance, CNR, and SNR compared with the 32-channel array (Fig. 11B).[44] While the form factor of this coil is somewhat bulky due to the D_2O-filled containers used to shorten element lengths, it remains somewhat flexible to conform to the chest wall. The characteristic transmit and receive profile of a dipole is very beneficial for cardiac imaging, as the transmit efficiency and sensitivity are lower at the surface and higher in deeper structures than loops,[45] therefore providing better field uniformity in this anteriorly positioned organ. It was reported that the gains in sensitivity allowed CINE acquisitions of $0.8 \times 0.8 \times 2.5\ mm^3$, which is 12-fold better than protocols used in clinical practice at 1.5T. These reported gains in resolution mirror the theoretical gains in sensitivity expected when progressing from 1.5 to 7T[1].

Although it is difficult to make a direct comparison in performance with the other arrays detailed in this section, several RF arrays to enhance transmit and receive performance with multiple different resonance structures have been presented. The loop-dipole transceiver array characterized above in the prostate section has been used in a variety of cardiovascular applications[46] (Fig. 11E). Then, there are 2 arrays that have loop-receiver arrays separate from the transmit elements. First is a cardiac-specific version of the 8-channel fractionated dipole with a 16-channel loop receiver (Fig. 11C).[49] By the addition of the 16 loops to the 8-channel dipole transceiver array, the SNR was increased 50% as in the previously reported prostate studies.[104] Second, is the array presented by Rietsch et al,[48] which, similar to the previous coil, consists of 8 blocks where each block is comprised of a meander transceiver and 3 receive-only loop elements (ie, 8Tx/32Rx) (Fig. 11D).

Coronary Magnetic Resonance Angiography (CMRA)

The potential of increased SNR, improved in-flow contrast, and increased acquisition speeds motivate the exploration of coronary artery imaging at UHF. At clinical field strengths (ie, 1.5 and 3.0T), acquisition methods developed to optimize CMRA contrast, resolution, and coverage cannot compete with the resolution and speed of computed tomography angiography (CTA). With the increased SNR and CNR at UHF, CMRA may be able to approach CTA resolutions while not requiring the use of contrast agents or ionizing radiation. The clinical motivation is to provide a sensitive diagnostic tool to detect and evaluate coronary artery stenosis and evaluate anomalous vessels.

Performing noncontrast right coronary artery (RCA) CMRA at 7T has been shown to improve the SNR, contrast to noise ratio (CNR), and vessel sharpness compared with 3T. Initial studies

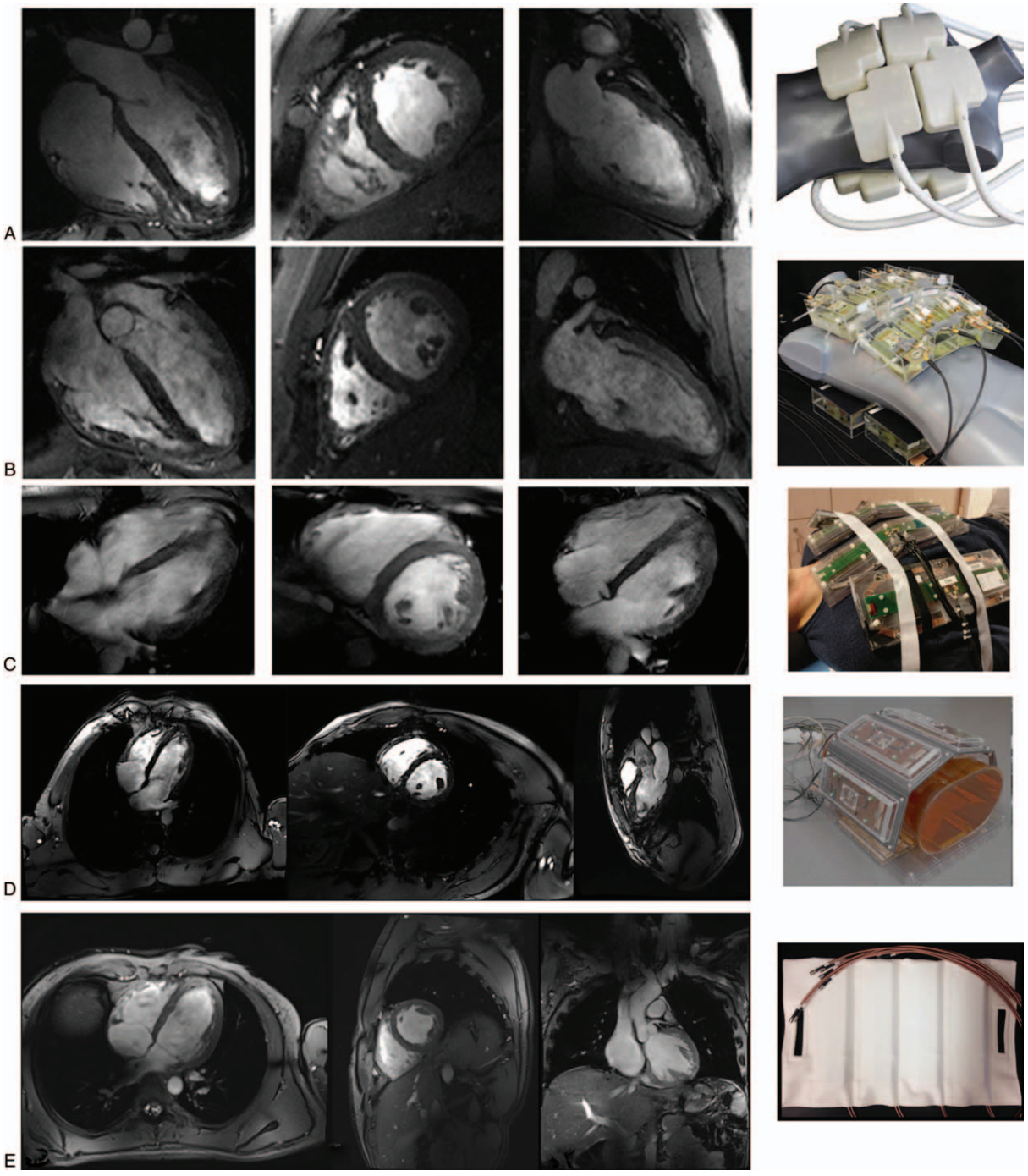

FIGURE 11. (A) A 32-channel transceiver array consisting of 8 building blocks comprised of 4 shielded loops in a 2×2 configuration per block. (B) An array comprised of 16 building blocks each containing a bow tie shaped $\lambda/2$-dipole antenna in a 4×2 configuration anterior and posterior (B). (A, B) employed a universal RF shim solution based on EM simulations implemented through a splitter to produce a uniform field in the 4-chamber view. Images for (A) and (B) are acquired with resolutions of $1.1 \times 1.1 \times 2.5\,mm^3$ and GRAPPA = 2 with acoustic cardiac triggering. (C), An 8-block array where each block is comprised of a fractionated dipole transceiver and 2 receive-only loops (ie, 8Tx/32Rx). The anterior elements are bent in the middle to better conform to the chest wall. Images were acquired with a resolution of $1.3 \times 1.3 \times 8\,mm^3$ with subject-dependent phase-based RF shimming and VCG gating. (D) An 8-block array where each block is comprised of a meander transceiver and 3 receive-only loop elements (ie, 8Tx/32Rx). RF shimming consisted of a universal phase-only RF shim and gating was performed with a finger pulse oximeter. Acquisition resolution was $1.5 \times 1.5 \times 3\,mm^3$ with GRAPPA = 2 acceleration. (E) Sixteen-channel transceiver array with 4 loop-dipole blocks both anterior and posterior driven by a 16-channel pTx-v1 system using subject-specific static RF shim optimized for homogeneity over the heart. Acquisition parameters were $1.2 \times 1.2 \times 4\,mm^3$ with GRAPPA = 2 and acquired with VCG gating. Images Courtesy of: Neindorf and Ozerdem (A,B); Steensma (C); Reitsch (D).

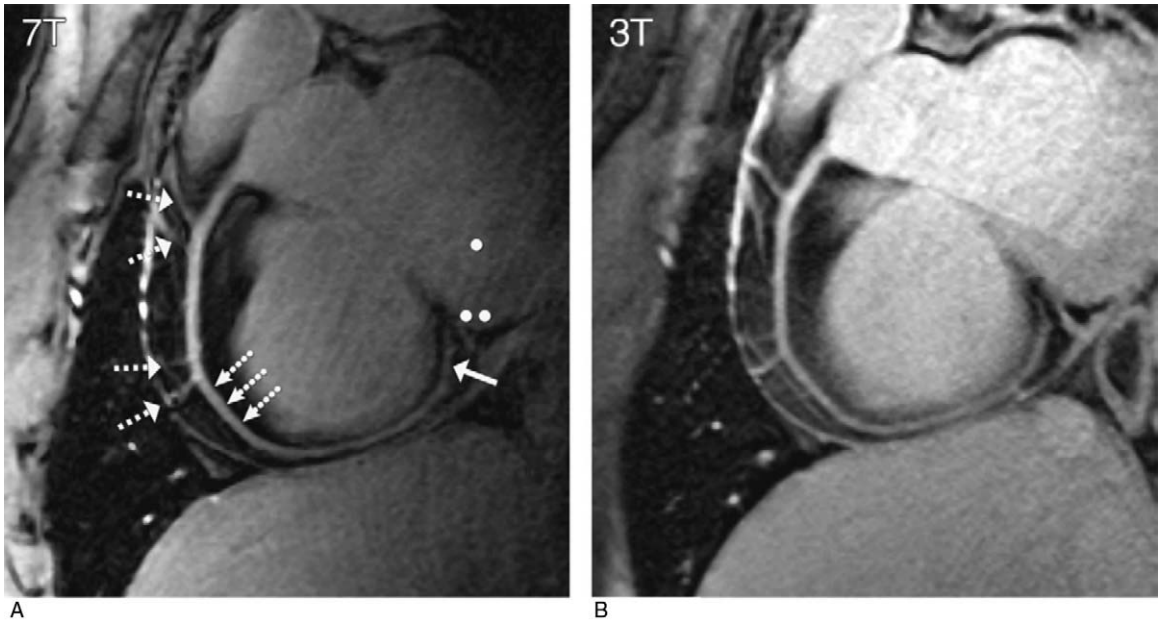

FIGURE 12. RCA images (double oblique volume targeted plane parallel to the RCA) in a healthy 26-year-old man display a high visual vessel definition (dotted arrows) in (A) the 7 T image compared with that at (B) 3 T. At 7 T, contrast is limited between the myocardium (••) and the blood pool (•). Multiple RCA side branches (dashed arrows) and distal parts of the RCA (solid arrow) are depicted clearly at both field strengths. Republished with permission of RSNA from van Elderen SG, Versluis MJ, Westenberg JJ, et al. ''Right coronary MR angiography at 7 T: a direct quantitative and qualitative comparison with 3 T in young healthy volunteers.'' *Radiology.* 2010;*257*(1):254-259.

demonstrated this advantage using a targeted 3D turbo-FLASH (TFL) acquisition with an adiabatic spectrally selective RF pre-pulse (SPAIR) for lipid suppression[145,146] (Fig. 12). Bizino et al[147] pushed the resolution in CMRA to find that acquired resolutions of $0.45 \times 0.45 \times 1.2$ were possible in the RCA and that the SNR dropped less than expected compared with a lower resolution acquisition. These initial studies made use of a quadrature transceiver loop coil, which had limited penetration into the chest. This RF coil was sufficient to image the RCA, which projects anteriorly from the aortic root and runs close to the chest wall.

To image the left coronary artery (LCA), better RF penetration and efficiency deep in the chest cavity were required. To address the challenge of low peak B_1^+ and the known challenge of B_1^+ inhomogeneity at 7T, multiple optimized B_1^+ shimming solutions within a single acquisition sequence were employed using a multichannel surface array coil.[22] The dynamically applied static shim solutions allowed for RF pulses within the sequence to be optimized not only in terms of their cost function but also in terms of their location. For these free-breathing acquisitions, a navigator is typically positioned on the diaphragm to both gate and track the acquisitions. For the navigator, the RF shimming was performed on a small region of the liver just inferior to the lung-liver interface optimized for efficiency providing a robust navigator signal (Fig. 13). A second ROI over the heart was used to optimize RF for lipid

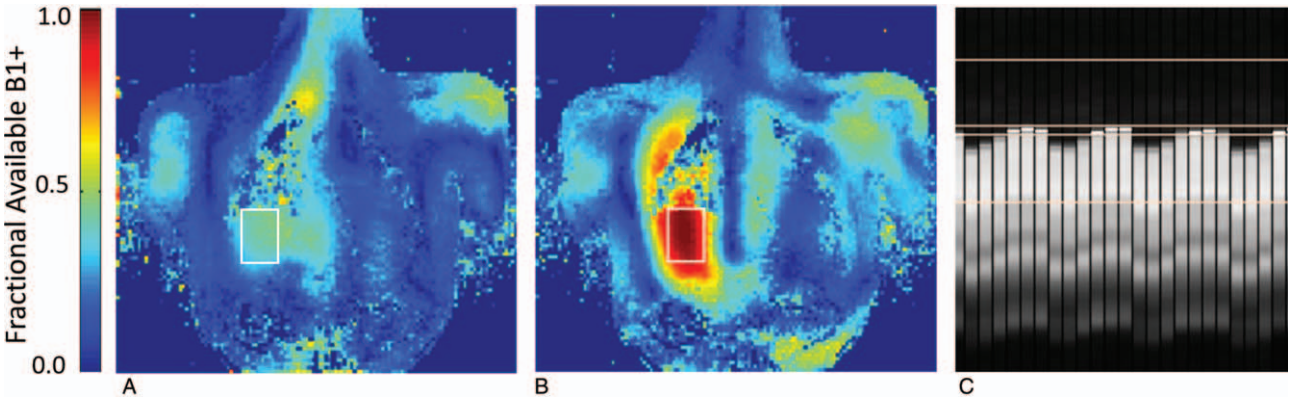

FIGURE 13. Dynamically applied RF shimming was used to improve performance of CMRA and 4D-flow imaging at 7T. In these sequences, high transmit efficiency was needed for the navigator to ensure a robust signal and sharp lung-liver interface for gating and tracking. Single breath-hold coronal calibration data were acquired for optimization in a target region located in the liver (white box). The fractional available B_1^+ (A) before and (B) after RF shimming show the high efficiency of phase-only static B_1^+ shimming for a small localized region. After RF shimming, a robust navigator signal can be obtained (C).

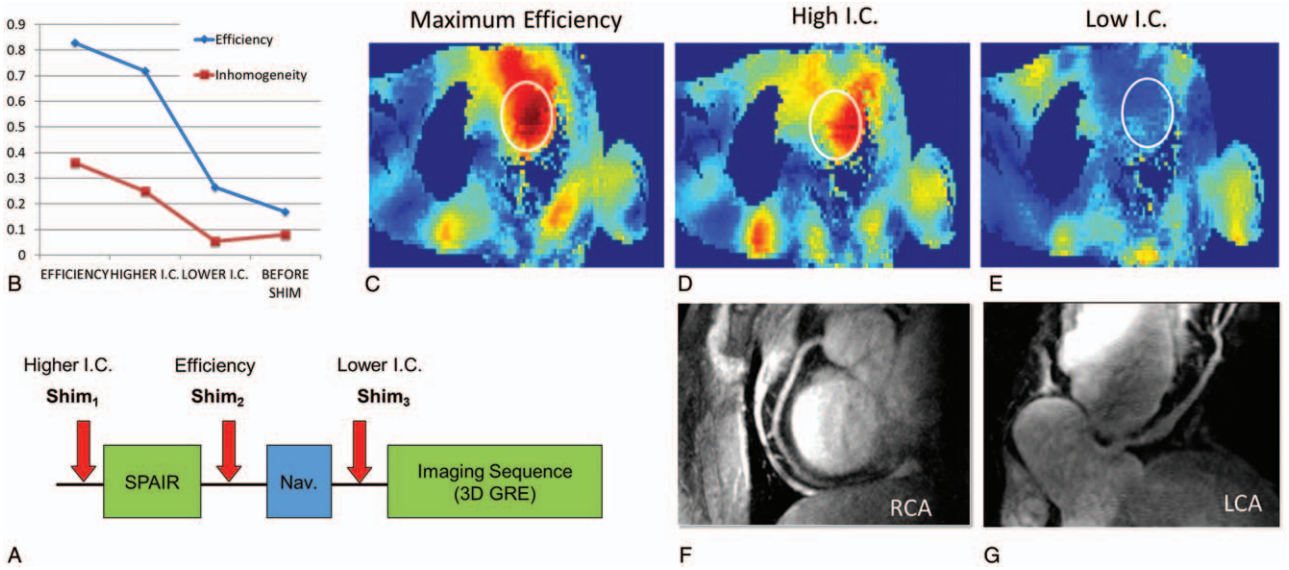

FIGURE 14. (A) Schematic of the CMRA sequence with dynamically applied static B_1^+ shimming for imaging of the left coronary artery. (B) Different RF shimming solutions in the target region of the heart (white ROI) demonstrate the tradeoff between efficiency and homogeneity where the inhomogeneity coefficient (I.C.) is given by the standard deviation over the mean. (C–E) Transmit efficiency maps for the shimming solutions shown in (B). As demonstrated in Fig. 13, an efficiency solution was used for the navigator, a higher I.C. solution for the lipid suppression and the most homogeneous solution was used for the low flip angle excitation of the gated GRE readout. Images of the (F) RCA and (G) LCA acquired with this strategy are shown.

suppression and the excitation of the GRE readout for various solutions trading off efficiency for homogeneity (Fig. 14). This strategy allowed the LCA to be imaged at 7T with similar contrast to that achieved in the RCA albeit with lower SNR due to the increased distance of the LCA from the RF coil. These acquisitions were acquired with a resolution of $0.8 \times 0.8 \times 2\,mm^3$.

As opposed to the RCA where it suffices to suppress epicardial fat, imaging the LCA has typically required a T2 magnetization preparation (T2-prep) to suppress the background myocardial signal. At 3T, it was required to make the T2-prep adiabatic versions to address B_1^+ inhomogeneities, but a similar strategy at 7T is impractical due to SAR limitations.[148] Further studies are needed to evaluate the relative performance of LCA visualization at 7T in comparison to 3T given these practical considerations; however, studies to date have been performed without any specific attempts to suppress the background myocardial signals.

Another option for CMRA includes the whole-heart acquisitions with or without contrast. The previous examples focused on smaller volume 3D acquisitions targeting sections of the left and/or right coronary arteries. Contrast-enhanced CMRA using blood pool agents has been shown to be an option for obtaining high fidelity whole heart CMRA at 3T using self-gated acquisitions. Such methods may also be promising at UHF. A preliminary study demonstrating contrast-enhanced MRA at 7T using self-gated UTE acquisition to minimize $T2^*$ effects has shown the feasibility of this strategy.[119]

4D Flow

Four-dimensional flow (4D Flow) refers to a time-resolved 3D GRE acquisition that provides phase-encoded velocity vectors in 3 directions allowing the spatiotemporal evaluation of blood flow. Its application in the aorta is promising for investigating changes in hemodynamics associated with aortic pathologies such as aortic valve disease, aneurysms, or dissections.[12] Limitations to its clinical application result from long acquisition times, partial volume effects, and compromised temporal resolution. These limitations can be addressed by exploiting the increased SNR of 7T where Hess et al[11,] reported a 1.8-fold and 2.2-fold increase in SNR at 7T compared with 3T with and without contrast, respectively.[12] This study employed an 8-channel transceiver stripline array on a pTx-v1 system at 7T. A dynamically applied static B_1^+ shim, similar to that used to acquire the LCA CMRA acquisitions, was detailed above. Two calibration scans were used to target 2 ROIs for shimming, one for the navigator at the lung-liver interface, and the other for the aorta. Both regions were optimized to maximize the minimum B_1^+. A second study conducted by Schmitter et al[149] focused on improving resolution and accelerating 4D flow acquisitions. In comparison to typical acquisitions of 2 to 3 mm in each direction, a resolution of 1.2 mm isotropic was possible with a 4.3-fold acceleration using kt-GRAPPA for an acquisition time of 11 minutes. Improved estimation of blood flow velocity and wall shear stress results from greater temporal and spatial resolutions. This study was performed with a 16-channel stripline array and a similar dynamically applied static shimming strategy as detailed above. With the availability of newer generation RF coils with improved receive sensitivity and coverage[44,46,48,49] along with spoke pulses to better tailor the available transmit fields, further improvements of 4D flow in the great vessels are anticipated with resolutions potentially providing access to smaller vessels in the heart and torso.

RENAL IMAGING

The potential role of UHF MRI in probing the anatomy and function of the kidneys has been previously described in the review by de Boer et al.[8] The noninvasive assessment of the kidneys has demonstrated clinical impact in assessing renal tumors, renal transplants, renal artery stenosis, acute kidney disease, and chronic kidney disease. Exploring the potential advantages of UHF in assessing the kidneys starts with the evaluation of basic hardware, acquisition methods, and validation studies, which have been the focus of the field to date. Beyond the methods detailed below, further developments in functional studies including blood oxygen level dependent

(BOLD) contrast with sensitivity to changes in blood flow and oxygenation have increased potential at UHF but require further development.[150,151]

Target-Specific Shimming

The native kidneys represent a unique target compared with the prostate and heart in terms of the challenges related to RF shimming. The kidneys, which are a bilateral structure sitting posterior in the torso, exhibit field inhomogeneities similar to the heart while also exhibiting deeper structure such as the descending aorta and origin of the renal arteries similar to the prostate. Multiple RF shimming strategies described above can be used depending on the RF pulses requirements in terms of RF homogeneity, efficiency, and spatial coverage. For general imaging of the overall anatomy, static B_1^+ shimming solutions are viable options if tailored to the kidneys or vessels, but it can also benefit from uniform cross-sectional imaging strategies aided by methods such as TIAMO.

Initial Studies

The first studies to explore renal anatomic and DCE-MRI at 7T were performed by Umutlu et al.[152,153] It was shown that GRE acquisitions with T1w contrast could depict anatomic structures and vasculature of the kidneys. However, T2w turbo spin echo (TSE) imaging suffered from a low and inhomogeneous B_1^+.[152] The same group later demonstrated the feasibility of DCE-MRI studies in the kidneys at 7T with a series of 3 images acquired post contrast to capture the arterial, venous, and post contrast phases.[153] These studies were acquired with an 8-channel transceiver array[37] using phase-based shimming with preset transmit modes for axial (CP+; 90° between channels) and coronal (CP; 45° between channels) acquisitions. It was noted that improvements in RF hardware and management were required to fully explore UHF renal studies.

Renal MRA

Renal vascular imaging has also been demonstrated at 7T in several studies both with and without exogenous contrast.[10,154–156] One study demonstrated that first pass contrast-enhanced renal MRA was feasible and provided improved SNR and CNR compared with noncontrast 3D T1w GRE acquisition when using the standard dose of Gd contrast agents of 0.1 mmol/kg bodyweight.[154] In subsequent studies, it was demonstrated that MRA studies using a quarter dose are diagnostic at 7T, although half and full dose studies provide better and near equivalent vessel visualization especially with the extra and intraparenchymal segmental arteries[156] (Fig. 15A).

Various strategies have been demonstrated for noncontrast-enhanced renal MRA.[10,155] Although low-dose contrast enhanced options are feasible, noncontrast imaging methods are highly desired for patients with renal insufficiency or when repeat scans are needed. Umutlu et al[155] compared a series of breathold acquisitions, including 2D T1w GRE, 3D T1w GRE, and time of flight (TOF) acquisitions. The 2D GRE and TOF acquisitions outperformed the 3D GRE both quantitatively and qualitatively. Meanwhile, TOF had the best background suppression and CNR but at the noted expense of venous signal contamination (Fig. 15B). In a subsequent study by Laader et al,[157] it was reported that TOF quantitatively outperformed low-dose CE renal MRA.

An alternative free-breathing renal MRA approach involves lipid suppression and magnetization preparation to suppress background signals.[10] Although the previous studies made use of an 8-channel transceiver array and standard transmit modes providing minimal B_1^+ inhomogeneities, the noncontrast free-breathing renal angiography study used a 16-channel transceiver array with dynamically applied static RF shimming using a pTx-v1 system. The noncontrast MRA sequence included an adiabatic inversion pulse to suppress the kidney parenchyma followed by lipid suppression and a small flip-angle GRE readout. To perform RF shimming, a calibration scan was performed with 3 slices through the kidneys. One ROI was drawn around the kidneys alone to determine an efficient solution for use with the adiabatic inversion. This pulse requires a relatively high peak B_1^+ while being relatively B_1^+ insensitive. The second ROI contained the kidneys and renal arteries in order to target a less efficient but more homogeneous RF shim. The homogeneous solution was used for the GRE readout as these pulses have much lower power requirements and it is the signal generated from this excitation that will determine the uniformity of the vessels in the final image. Acquisitions were acquired in <10 minutes at a resolution of 1.0 to 1.2 mm isotropic with respiratory triggering using a standard monitoring belt (Fig. 15C). In addition to the increased SNR at 7T, the longer T1 of the parenchyma prolongs the inversion time for parenchymal suppression allowing for increased filling of the vasculature compared with lower field strengths. The potential benefits include improved visualization of the first- and second-order branches as well as more distal arteries compared with lower field strengths and contrast-enhanced acquisitions.

Relaxometry

Knowledge of the renal relaxation rates is beneficial for sequence optimization, as a baseline for assessing disease state and as prior knowledge when estimating renal perfusion from ASL data. A single breath-hold relaxometry study, comparing the T1 and T2 in the renal cortex and medulla, was conducted by Li et al[9] using a single-shot magnetization-prepared fast spin echo (ss-FSE) acquisition. For T1 mapping, an adiabatic inversion pulse was applied with varying delays. For T2 mapping, a Carr-Purcell-Meiboom-Gill (CPMG) style refocused pulse train of varying lengths was utilized. To most effectively use the available B_1^+, static RF shimming was focused on an axial slice of a single kidney optimized to balance B_1^+ homogeneity and RF efficiency. The acquisitions were accomplished with a 16-channel stripline array coil on a pTx-v1 system at 7T. In the cortex, T1 values increased from 1261 to 1647 ms and T2 values decreased from 128 to 107 ms in the cortex at 3T and 7T, respectively. In the medulla, T1 values increased from 1676 to 2092 ms and T2 values decreased from 128 to 124 ms at 3T and 7T, respectively.

ARTERIAL SPIN LABELING

Arterial spin labeling is an MRI technique to measure perfusion without the need for exogenous contrast agents. Instead, RF-labeled water in upstream blood is used as a freely diffusible tracer. Experiments are run with and without labeling and the difference images are processed with kinetic models to derive blood flow. The increased SNR and prolonged T1 of 7T can benefit ASL studies by improving the achievable resolution, decreasing the required acquisition time, and permitting longer post bolus delay times as needed in organs with long arterial transit times or for reducing intravascular effects.

In the kidney, a flow-sensitive alternating inversion recovery (FAIR) method was employed for ASL perfusion imaging of the kidney at 7T.[71] The acquisition consisted of FAIR preparation followed by a single-shot fast spin echo (ss-FSE) readout. The FAIR ss-FSE sequence consists of a pre-saturation RF pulse targeting the location and extent of the oblique coronal imaging slice followed by an inversion RF pulse centered on the coronal imaging slice but alternating between a narrow slab covering the imaging slice or a lager slab including the feeding vessels. A 2-solution dynamically applied RF shimming strategy was implemented for the management of B_1^+. In this study, a multi-delay study was performed to determine the temporal bolus needed for the more time-efficient single subtraction study and to validate the single subtraction study results. The

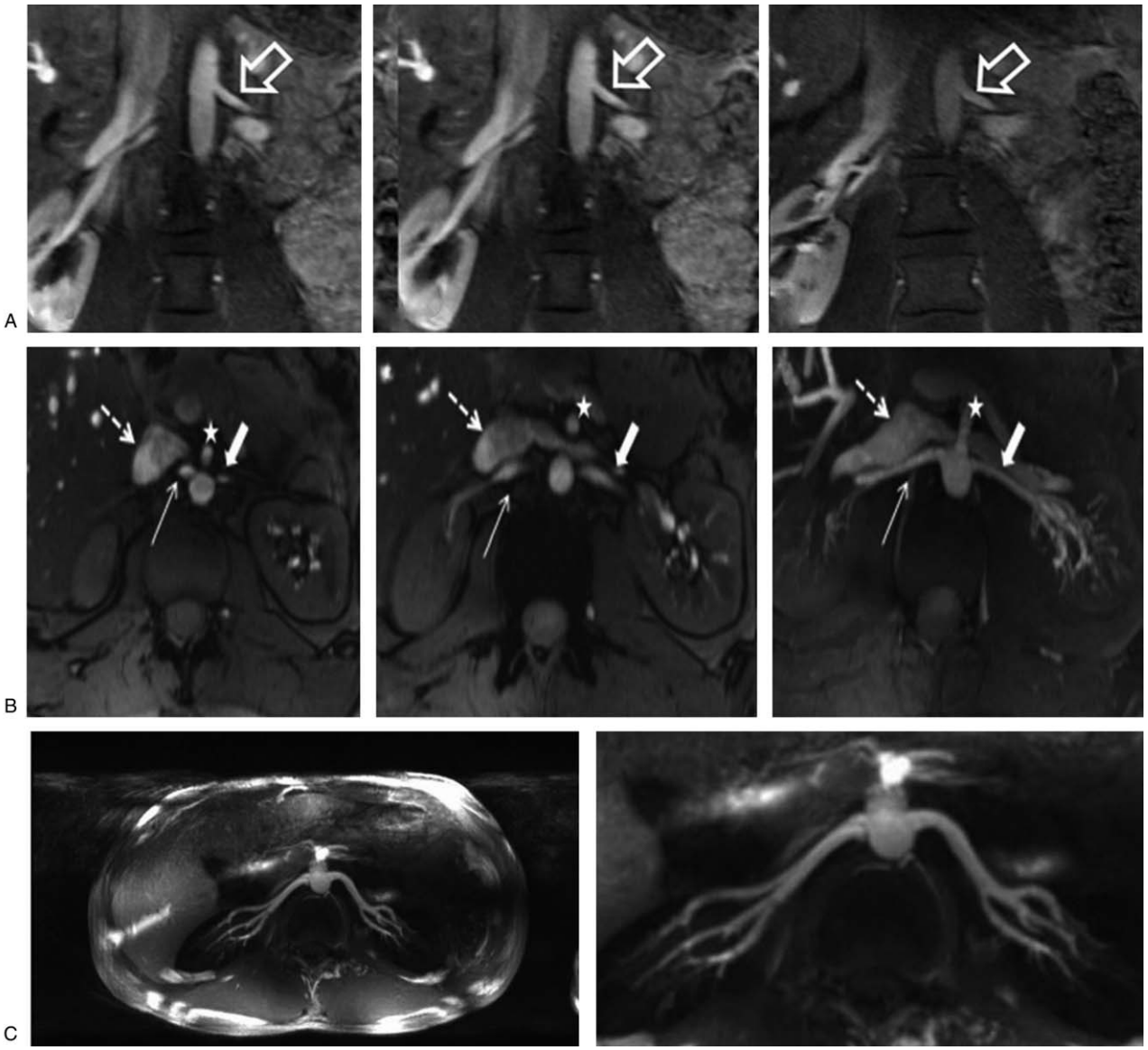

FIGURE 15. Left renal artery at 3 different gadolinium doses (A-left: 0.1 mmol/kg bodyweight; A-middle: 0.05 mmol/kg bodyweight; A-right: 0.025 mmol/kg bodyweight). All 3 gadolinium doses allow for a hyperintense vessel signal, with higher vessel contrast at the higher gadolinium doses. TOF MRA (B-left, B-middle) and maximum intensity projection (MIP) of TOF MRA (B-right) provide excellent delineation of both renal arteries in full extent from proximal to peripheral segments (broad arrow: left renal artery; slim arrow: right renal artery). Due to general hyperintense vasculature signal intensity, moderate venous overlay is apparent (dashed arrow: inferior cava vein; white dashed arrow: left renal vein). White star points to partially depicted superior mesenteric artery. Thin axial MIPs (C-left) and zoomed coronal MIPs (C-right) of 3D free-breathing renal MRA. Dynamically applied static B_1^+ shimming was used with a tradeoff between efficiency and homogeneity for inversion and homogeneous solution using magnitude and phase optimization for excitation. (A) Reproduced with permission of Elsevier Ireland LTD from Beiderwellen et al.[156] (B) Reproduced with permission of John Wiley and Sons from Umutlu et al.[155] (C) Adapted with permission from John Wiley and Sons from Metzger et al.[10]; permissions conveyed through Copyright Clearance.

temporal bolus width at 7T of 600 ms was shorter than that at 3T. The difference results from the fact that the 3T system uses a whole-body transmitter and at 7T we have local transceiver arrays, thus a smaller fraction of the blood pool is labeled at 7T. Because of the longer T1 of blood at UHF, the total post bolus delay could be set at 1200 ms to minimize intravascular effects. Quantitative renal blood perfusion was possible with the proposed methods within SAR limits in a single breath-hold. Further studies have shown that 7T is superior to 3T for renal perfusion imaging using a similar approach[158] (Fig. 16). Along with prolonged repetitions times of 4 seconds, other management strategies to decrease local SAR included variable-rate selective excitation (VERSE) pulses for excitation,[159] hyperechoes for the FSE readout,[160] and gradient offset independent adiabatic (GOIA)[161] pulses for label and control inversions.

Similar acquisition and RF management strategies have been applied in preliminary ASL studies in the heart[162] and the prostate[72]

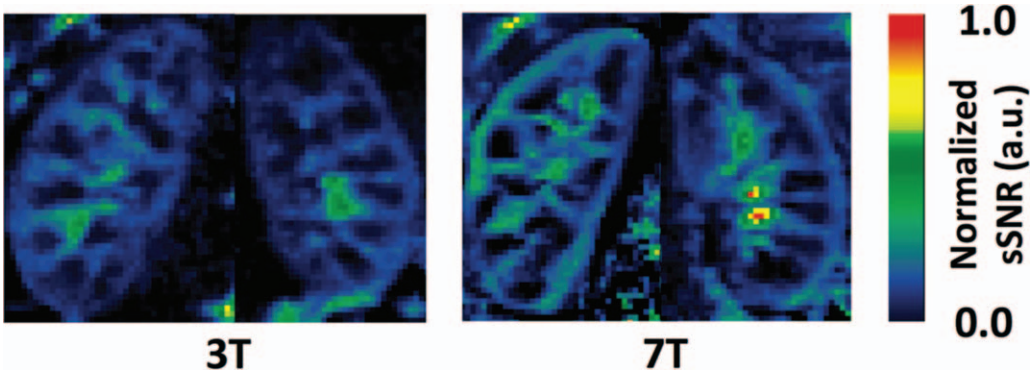

FIGURE 16. Normalized spatial SNR (sSNR) maps of 1 representative subject from single breath-hold FAIR ss-FSE imaging at 3T (left) and 7T (right).

at 7T. For the heart, there was the additional challenge of cardiac triggering, but the TSE readout helped to minimize the deleterious effects of an inhomogeneous and time-varying B_0. In comparison to 3T, the 7T cardiac ASL had a consistent increase in perfusion SNR. For the prostate, the long arterial transit times require a long post bolus delay, which is supported by the persistent labeling present due to the prolonged T1 at 7T. Combined with appropriate B_1^+ shimming strategies, prostate ASL imaging at 7T has been previously demonstrated[163] (Fig. 17).

ABDOMINAL IMAGING

Liver

Dynamic contrast enhanced hepatic MRI has been a powerful technique for evaluation of liver disease and assessment of liver vessel pathologies. Initial contrast-enhanced liver MRI studies at 7T provided high-quality T1-weighted images; however, T2-weighted imaging was compromised by severe B_1^+ nonuniformities.[164,165] Noncontrast imaging at of the hepatic arterial vasculature was also successfully demonstrated, capitalizing on the hyperintense vessel signals at 7T.[165] In a study by Laader et al,[166] 1.5, 3, and 7T MRI were compared in 10 healthy subjects demonstrating higher spatial resolution for nonenhanced vessel imaging at 7T, but inferior T2-weighted acquisitions. While demonstrating the promise of UHF liver imaging, RF was transmitted through a multichannel transceiver array with a fixed transmit mode as opposed to subject-specific or target-specific RF shimming.

As the liver is the largest parenchymal organ in the torso, achieving a uniform B_1^+ distribution in the entire organ is challenging due to its size and relatively high relative permittivity ($\varepsilon_r > 50$). Static RF shimming approaches are found to be insufficient to uniformly image this anatomical target. Employing strategies such as TIAMO or dynamic RF shimming strategies may greatly improve the applications that can be performed at 7T in the liver. For example, uniform liver imaging was demonstrated by Wu et al[64] utilizing multi-spoke excitation pulses (Fig. 3).

Other Anatomies

The SNR of a monopole antenna increases quadratically with B_0,[167] making it an attractive minimally invasive receiver option to boost SNR at UHF. Hoogendam et al[168] employed an endorectal monopole antenna in combination with an external surface array to perform cervical MRI at 7T. Follow-up work by Arteaga de Castro et al[169] obtained lipid profiles in cervical carcinomas with 1H MRS and demonstrated that 2.1 ppm/1.3 ppm fatty acid ratio might be associated with tumor grade.

Initial 7T small bowel imaging studies were performed in a comparative manner against clinical 1.5T MRI. Initial T1-weighted

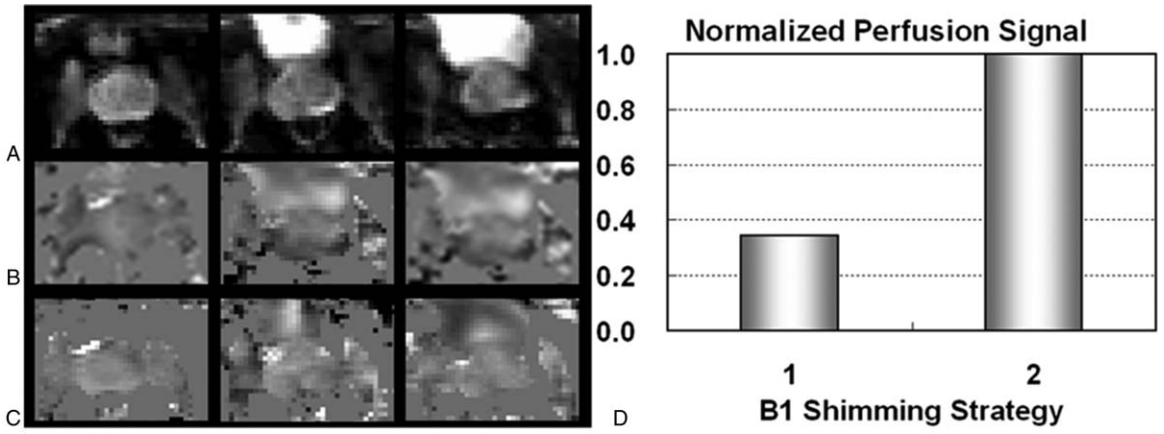

FIGURE 17. Prostate perfusion imaging results from a subject acquired at 7T. Shown are proton density images at three locations (A) followed by perfusion-weighted imaging maps acquired with a fixed single B_1^+ shimming solution (B) and dynamically applied multiple B_1^+ shimming solutions (C). (D) Normalized prostate perfusion signals are presented using the two B_1^+ shimming strategies: strategy 1) using a single B_1^+ shim optimized for efficiency on the prostate, and strategy 2) using multiple dynamically applied B1 shimming solutions for different RF components.

and noncontrast-enhanced 7T MRI demonstrated comparable imaging performance with 1.5T,[170,171] while technical advances at 7T are needed to reach its full potential.

DISCUSSION

This review covers specific historical aspects of proton torso imaging and spectroscopy at UHF with a primary focus on the technological developments that have allowed multiple applications to be explored. This is by no means a comprehensive review of all aspects of UHF body imaging below the head. Significant advances in breast and musculoskeletal applications will be the subject of dedicated reviews. Multinuclear applications are also not covered however, it is widely understood that the increased sensitivity at UHF is critical for the expanded utility of sodium, phosphorus, and other nuclei. These low-gamma nuclei do not have the same issues as protons due to the fact their wavelengths are much longer by comparison. At the same time, deploying acquisition resources for these nuclei involves a different set of technical challenges that warrant dedicated coverage.

Transmit Chain

The increased degrees of freedom afforded by multichannel transmit coils and pTx-v2 systems not only present a unique opportunity to overcome many challenges at UHF but also contribute to its complexity. While representing a critical first step demonstrating the highly promising potential of pTX, the first-generation pTx-v2 systems also suffered from issues arising in part from the challenging integration of 8 to 16 complete transmit chains, from the needs for updated imaging methods and new multichannel calibration resources, and from lingering limitations in realizing the performance advantages of real-time local SAR monitoring. Regarding more advanced systems, commercial options that are far more compact and integrated are already available and there is little doubt that they will be gradually adopted in the field. Driven by more integrated pTx systems, the acquisition methods will follow. Meanwhile, strategies to alleviate the bottleneck resulting from channel-dependent B_1^+ calibration are already being used in practice[61–63,172] and newly proposed methods with advantages for body applications have been published.[173] As a way to limit the burden of acquiring subject/target-specific calibration data, universal pulse strategies are also an option but have yet to be explored for applications outside the brain.[68,69,174] With respect to real-time local SAR monitoring, it is possible to design pulses,[175] sequences,[10,74] and imaging sessions that purposefully reduce local SAR. Continued work is needed investigating the relevance of EM simulations performed in body models that do not match the specific subject being imaged. These studies are critical to help optimize limits on power deposition so that they are not overly conservative to the degree that the benefits of local SAR monitoring are lost.

Further developments of pTx-v2 systems and calibration methods will allow RF pulse optimization to perform local excitation as well as RF shimming. Multidimensional selective pulses can allow for reduced field of view imaging. Given the increased SNR at UHF, which supports higher resolutions, a way to decrease scan time is to reduce the effective FOV that needs to be encoded. Another advantage of exciting spins within a limited target anatomy is that artifacts resulting from motion of tissue beyond the region of interest can be reduced. An example of reduced FOV imaging has been demonstrated in the spine[176] and kidney at 7T.[177]

RF Shimming

The inherently contradictory goals of transmit efficiency and homogeneity make it challenging to simultaneously use the limited available RF power effectively when attempting to obtain high-quality images while not exceeding local SAR limits. Compared with head applications where reasonable peak B_1^+ can be obtained, the limited peak achievable B_1^+ in body imaging at UHF has been, until now, a very serious limitation. As our understanding and implementation of real-time local SAR monitoring progresses, there will be more flexibility to utilize systems with higher total available RF power for these applications.

With current amplifier configurations and pTx-v1 systems, we are typically limited to 16 kW of total power in either 16×1 kW or 8×2 kW configurations, keeping in mind that about typically 50% of RF power is lost in the tens of meters of cable running between the RF amplifiers and the RF coil. RF shimming using these systems just barely provides the B_1^+ needed to acquire multiparametric data, including T2w FSE images, in the prostate using local transmit arrays. In larger anatomies, it was shown that image quality can be greatly compromised when a proper RF transmit chain, RF coil, and target-specific shimming are not used in concert. For more advanced applications, dynamically applied static RF shimming was critical to the methods success. It was important to use an efficiency solution to improve navigator performance in 4D-flow[12] and angiography studies[10,22] and to maintain labeling efficiency in ASL studies[10,71] while using a more uniform B_1^+ in the imaging volume. As implemented, the calibration data needed to perform the RF shimming solutions involved 1 or 2 breath-holds. An obvious extension of this strategy would be to dynamically apply *dynamic* RF shims.

RF Coils

The presented studies have demonstrated that RF coils for imaging in the torso can greatly benefit from the flexibility of having multiple independent transmit channels to facilitate RF shimming and even more receiver channels for improved SNR and parallel imaging performance. Although promising developments in integrated whole-body transmitters are being achieved,[178,179] the complexity, expense, and increased total available power requirements of such systems will make local transmitters a preferred transmit configuration in many applications. On the receive side, receive-only elements along with transceiver elements within a coil also appear to be the desired approach to maximize both transmit and receive performance.[49,180]

Coils with separate receivers have the potential to compete with coils optimized for receive that are typically used at lower field strengths. Without optimizing this aspect of performance, potential gains in terms of SNR may not be realized. The general torso arrays with several rows of receive-only elements along the foot-head direction[49,180] and those cardiac specific arrays with similar distributions of transceiver elements along the z-axis[40,41,44] show great potential to further increase parallel imaging acceleration in multiple slice orientations.

Safety

Although not specific to the body, the need for extending access is critical to growth in the field. Providing safe options for individuals with metallic implants would be necessary. Reducing local SAR or heating around implants can be improved by using pTx to mitigate heating resulting from induced currents in conductive implants.[181–184] It is worth noting that local transmit arrays may alleviate the risk of RF heating if the implanted device resides away from the imaging FOV (ie, outside the region of the body in which the majority of energy is being deposited). Large variations in transmit coils and shimming strategies employed in different UHF sites and their continuous evolution necessitate implanted device evaluation on a case-by-case basis to determine safe operating conditions based on coil design, transmit shim setting, scan location, and coil position. Initial reports on implant and tattoo safety and laboratory-specific

experiences are important for establishing the new norms for imaging at UHF ([26], and references therein).

CONCLUSION

The iterative development of body imaging applications and the technology that makes it possible continue at 7T. Although the development of high field systems has been driven by applications focusing on neuroanatomy and function, the feasibility and advantages of imaging targets throughout the torso have already been demonstrated. Although some applications require rather complex hardware and optimization to perform, it is time to push the field forward by recognizing and exploring the potential benefit of performing these studies at 7T and higher. Acknowledging the benefit of UHF in research and clinical applications will drive further technological developments to streamline what are now complex and time-consuming procedures. Advances will occur even more quickly if body imaging at 7T receives regulatory approval so that the exploration of clinical applications that benefit from UHF and the development of technology to make those explorations possible become mutually motivating.

ACKNOWLEDGMENTS

The authors would like to acknowledge all the pioneers in the field and especially those who have contributed material presented in this review: Thomas J. Vaughan (University of Columbia, New York, USA), Xiaoping Wu (University of Minnesota, Minneapolis USA); Bart Philips (Radboud University Medical Center, Nijmegen, the Netherlands); Joseph Suttie (Riverina Cardiology, Wagga Wagga, Australia); Thoralf Niendorf and Celal Oezerdem (Berlin Ultrahigh Field Facility, Berlin, Germany); Bart Steensma (University Medical Center Utrecht, Utrecht, the Netherlands); Andrew Webb (Leiden University Medical Center, Leiden, the Netherlands); Stefan Rietsch, Karsten Beiderwellen and Lale Umutlu (Erwin L. Hahn Institute for MR Imaging, University of Duisburg-Essen, Essen, Germany).

REFERENCES

1. Pohmann R, Speck O, Scheffler K. Signal-to-noise ratio and MR tissue parameters in human brain imaging at 3, 7, and 9.4 tesla using current receive coil arrays. *Magn Reson Med*. 2016;75:801–809.
2. Erturk MA, Wu X, Eryaman Y, et al. Toward imaging the body at 10.5 tesla. *Magn Reson Med*. 2017;77:434–443.
3. Wiesinger F, Van de Moortele PF, Adriany G, et al. Parallel imaging performance as a function of field strength: an experimental investigation using electrodynamic scaling. *Magn Reson Med*. 2004;52:953–964.
4. Frischer JM, God S, Gruber A, et al. Susceptibility-weighted imaging at 7 T: improved diagnosis of cerebral cavernous malformations and associated developmental venous anomalies. *Neuroimage Clin*. 2012;1:116–120.
5. Tkac I, Oz G, Adriany G, et al. In vivo 1H NMR spectroscopy of the human brain at high magnetic fields: metabolite quantification at 4T vs. 7T. *Magn Reson Med*. 2009;62:868–879.
6. Metzger GJ, Auerbach EJ, Warlick CA, et al. Evaluation of improved spatial and spectral resolution on model based fitting of prostate spectroscopy at 7 Tesla. *Proc Intl Soc Mag Reson Med*. 2012;20:4390.
7. Liu G, Song X, Chan KW, et al. Nuts and bolts of chemical exchange saturation transfer MRI. *NMR Biomed*. 2013;26:810–828.
8. de Boer A, Hoogduin JM, Blankestijn PJ, et al. 7 T renal MRI: challenges and promises. *MAGMA*. 2016;29:417–433.
9. Li X, Bolan PJ, Ugurbil K, et al. Measuring renal tissue relaxation times at 7 T. *NMR Biomed*. 2015;28:63–69.
10. Metzger GJ, Auerbach EJ, Akgun C, et al. Dynamically applied B1+ shimming solutions for non-contrast enhanced renal angiography at 7.0 Tesla. *Magn Reson Med*. 2013;69:114–126.
11. Hess AT, Bissell MM, Ntusi NA, et al. Aortic 4D flow: quantification of signal-to-noise ratio as a function of field strength and contrast enhancement for 1.5T, 3T, and 7T. *Magn Reson Med*. 2015;73:1864–1871.
12. Schmitter S, Schnell S, Ugurbil K, et al. Towards high-resolution 4D flow MRI in the human aorta using kt-GRAPPA and B1+ shimming at 7T. *J Magn Reson Imaging*. 2016;44:486–499.
13. Glover GH, Hayes CE, Pelc NJ, et al. Comparison of linear and circular-polarization for magnetic-resonance imaging. *J Magn Reson*. 1985;64:255–270.
14. Bottomley PA, Andrew ER. RF magnetic field penetration, phase shift and power dissipation in biological tissue: implications for NMR imaging. *Phys Med Biol*. 1978;23:630–643.
15. Yang QX, Wang JH, Zhang XL, et al. Analysis of wave behavior in Lossy dielectric samples at high field. *Magn Reson Med*. 2002;47:982–989.
16. Kangarlu A, Baertlein BA, Lee R, et al. Dielectric resonance phenomena in ultra high field MRI. *J Comput Assist Tomogr*. 1999;23:821–831.
17. Van de Moortele PF, Akgun C, Adriany G, et al. B(1) destructive interferences and spatial phase patterns at 7 T with a head transceiver array coil. *Magn Reson Med*. 2005;54:1503–1518.
18. International Electrotechnical Commission (IEC). Medical electrical equipment - Part 2-33: Particular requirements for the Safety of Magnetic Resonance Equipment for Medical Diagnosis. International Standard IEC 60601-2-33:2010.
19. Hoffmann J, Henning A, Giapitzakis IA, et al. Safety testing and operational procedures for self-developed radiofrequency coils. *NMR Biomed*. 2016;29:1131–1144.
20. Arteaga de Castro CS, Boer VO, Luttje MP, et al. Temporal B0 field variation effects on MRSI of the human prostate at 7 T and feasibility of correction using an internal field probe. *NMR Biomed*. 2014;27:1353–1360.
21. Schmitter S, Wu X, Ugurbil K, et al. Design of parallel transmission radiofrequency pulses robust against respiration in cardiac MRI at 7 Tesla. *Magn Reson Med*. 2015;74:1291–1305.
22. Metzger GJ, DelaBarre L, Bi X, et al. Left coronary artery imaging at 7T: initial results using multiple B1+ shimming algorithms and targets. *Proc Intl Soc Mag Reson Med*. 2011;19:116.
23. Vaughan JT, Snyder C, DelaBarre L, et al. 7T body imaging: first results. *Proc Intl Soc Mag Reson Med*. 2006;16:213.
24. Umutlu L, Ladd ME, Forsting M, et al. 7 Tesla MR imaging: opportunities and challenges. *Rofo*. 2014;186:121–129.
25. Trattnig S, Bogner W, Gruber S, et al. Clinical applications at ultrahigh field (7T). Where does it make the difference? *NMR Biomed*. 2016;29:1316–1334.
26. Kraff O, Quick HH. 7T: physics, safety, and potential clinical applications. *J Magn Reson Imaging*. 2017;46:1573–1589.
27. Niendorf T, Sodickson DK, Krombach GA, et al. Toward cardiovascular MRI at 7 T: clinical needs, technical solutions and research promises. *Eur Radiol*. 2010;20:2806–2816.
28. Niendorf T, Paul K, Oezerdem C, et al. W(h)ither human cardiac and body magnetic resonance at ultrahigh fields? Technical advances, practical considerations, applications, and clinical opportunities. *NMR Biomed*. 2016;29:1173–1197.
29. Stab D, Al Najjar A, O'Brien K, et al. Cardiac magnetic resonance imaging at 7 Tesla. *J Vis Exp*. 2019. doi: 10.3791/55853.
30. Vaughan JT, Adriany G, Snyder CJ, et al. Efficient high-frequency body coil for high-field MRI. *Magn Reson Med*. 2004;52:851–859.
31. Willinek WA, Gieseke J, Kukuk GM, et al. Dual-source parallel radiofrequency excitation body MR imaging compared with standard MR imaging at 3.0 T: initial clinical experience. *Radiology*. 2010;256:966–975.
32. Vaughan JT, Snyder CJ, DelaBarre LJ, et al. Whole-body imaging at 7T: preliminary results. *Magn Reson Med*. 2009;61:244–248.

33. Snyder CJ, DelaBarre L, Tian J, et al. 28-channel receive-only array for body imaging at 7T. *Proc Intl Soc Mag Reson Med*. 2010;18:3839.
34. Snyder CJ, DelaBarre L, Metzger G, et al. 32-channel receive only array for cardiac imaging at 7T. *Proc Intl Soc Mag Reson Med*. 2011;19:7375.
35. Orzada S, Bitz AK, Johst S, et al. Analysis of an integrated 8-channel Tx/Rx body array for use as a body coil in 7-Tesla MRI. *Front Phys*. 2017;5:1–10.
36. Paska J, Cloos MA, Wiggins GC. A rigid, stand-off hybrid dipole, and birdcage coil array for 7 T body imaging. *Magn Reson Med*. 2018;80:822–832.
37. Orzada S, Quick HH, Ladd ME, et al. A flexible 8-channel transmit/receive body coil for 7 T human imaging. *Proc Intl Soc Mag Reson Med*. 2009;17:3010.
38. Raaijmakers AJ, Ipek O, Klomp DW, et al. Design of a radiative surface coil array element at 7 T: the single-side adapted dipole antenna. *Magn Reson Med*. 2011;66:1488–1497.
39. Snyder CJ, Delabarre L, Moeller S, et al. Comparison between eight- and sixteen-channel TEM transceive arrays for body imaging at 7 T. *Magn Reson Med*. 2012;67:954–964.
40. Winter L, Kellman P, Renz W, et al. Comparison of three multichannel transmit/receive radiofrequency coil configurations for anatomic and functional cardiac MRI at 7.0T: implications for clinical imaging. *Eur Radiol*. 2012;22:2211–2220.
41. Graessl A, Renz W, Hezel F, et al. Modular 32-channel transceiver coil array for cardiac MRI at 7.0T. *Magn Reson Med*. 2014;72:276–290.
42. Ipek O, Raaijmakers AJ, Lagendijk JJ, et al. Intersubject local SAR variation for 7T prostate MR imaging with an eight-channel single-side adapted dipole antenna array. *Magn Reson Med*. 2014;71:1559–1567.
43. Rosenkrantz AB, Zhang B, Ben-Eliezer N, et al. T2-weighted prostate MRI at 7 Tesla using a simplified external transmit-receive coil array: correlation with radical prostatectomy findings in two prostate cancer patients. *J Magn Reson Imaging*. 2015;41:226–232.
44. Oezerdem C, Winter L, Graessl A, et al. 16-channel bow tie antenna transceiver array for cardiac MR at 7.0 tesla. *Magn Reson Med*. 2016;75:2553–2565.
45. Raaijmakers AJ, Italiaander M, Voogt IJ, et al. The fractionated dipole antenna: a new antenna for body imaging at 7 Tesla. *Magn Reson Med*. 2016;75:1366–1374.
46. Erturk MA, Raaijmakers AJ, Adriany G, et al. A 16-channel combined loop-dipole transceiver array for 7 Tesla body MRI. *Magn Reson Med*. 2017;77:884–894.
47. Adriany G, Van de Moortele PF, Wiesinger F, et al. Transmit and receive transmission line arrays for 7 Tesla parallel imaging. *Magn Reson Med*. 2005;53:434–445.
48. Rietsch SHG, Orzada S, Maderwald S, et al. 7T ultra-high field body MR imaging with an 8-channel transmit/32-channel receive radiofrequency coil array. *Med Phys*. 2018;45:2978–2990.
49. Steensma BR, Voogt IJ, Leiner T, et al. An 8-channel Tx/Rx dipole array combined with 16 Rx loops for high-resolution functional cardiac imaging at 7 T. *MAGMA*. 2018;31:7–18.
50. Padormo F, Beqiri A, Hajnal JV, et al. Parallel transmission for ultrahigh-field imaging. *NMR Biomed*. 2016;29:1145–1161.
51. Vaughan JT, Adriany G, Ugurbil K, Inventors; Univeristy of Minnesota, assignee. Shim, gradient, and parallel imaging coil. US patent 7,268,554; 2003.
52. Vaughan T, DelaBarre L, Snyder C, et al. 9.4T human MRI: preliminary results. *Magn Reson Med*. 2006;56:1274–1282.
53. Hoult DI, Phil D. Sensitivity and power deposition in a high-field imaging experiment. *J Magn Reson Imaging*. 2000;12:46–67.
54. Metzger GJ, van de Moortele PF, Akgun C, et al. Performance of external and internal coil configurations for prostate investigations at 7 T. *Magn Reson Med*. 2010;64:1625–1639.
55. Bitz AK, Orzada S, Kraff O, et al. An 8-channel add-on RF shimming system for whole-body 7 Tesla MRI including real-time SAR monitoring. *Proc Intl Soc Mag Reson Med*. 2009;17:4767.
56. Ibrahim TS, Lee R, Abduljalil AM, et al. Dielectric resonances and B(1) field inhomogeneity in UHFMRI: computational analysis and experimental findings. *Magn Reson Med*. 2001;19:219–226.
57. Eichfelder G, Gebhardt M. Local specific absorption rate control for parallel transmission by virtual observation points. *Magn Reson Med*. 2011;66:1468–1476.
58. Adriany G, Van de Moortele PF, Ritter J, et al. A geometrically adjustable 16-channel transmit/receive transmission line array for improved RF efficiency and parallel imaging performance at 7 Tesla. *Magn Reson Med*. 2008;59:590–597.
59. Metzger GJ, Snyder C, Akgun C, et al. Local B1+ shimming for prostate imaging with transceiver arrays at 7T based on subject-dependent transmit phase measurements. *Magn Reson Med*. 2008;59:396–409.
60. Snyder CJ, DelaBarre L, Metzger GJ, et al. Initial results of cardiac imaging at 7 Tesla. *Magn Reson Med*. 2009;61:517–524.
61. Van de Moortele PF, Snyder C, DelaBarre L et al. Fast Mapping of Relative B1+ Phase in the Human Head at 9.4 Tesla with a 14 Channel Transceive Coil Array. Intnl Symp on Biom Magn Reson Imag and Spectr at Very High Fields; Wuerzburg 2006; 37.
62. Van de Moortele PF, Snyder C, DelaBarre L, et al. Calibration tools for RF shim at very high field with multiple element RF coils: from ultra fast local relative phase to absolute magnitude B1+ mapping. *Proc Intl Soc Mag Reson Med*. 2007;15:1676.
63. Van de Moortele P, Ugurbil K. Very fast multi channel B1 calibration at high field in the small flip angle regime. *Proc Intl Soc Mag Reson Med*. 2009;17:367.
64. Wu X, Schmitter S, Auerbach EJ, et al. Mitigating transmit B 1 inhomogeneity in the liver at 7T using multi-spoke parallel transmit RF pulse design. *Quant Imaging Med Surg*. 2014;4:4–10.
65. Schmitter S, Moeller S, Wu X, et al. Simultaneous multislice imaging in dynamic cardiac MRI at 7T using parallel transmission. *Magn Reson Med*. 2017;77:1010–1020.
66. Schmitter S, DelaBarre L, Wu X, et al. Cardiac imaging at 7 Tesla: single- and two-spoke radiofrequency pulse design with 16-channel parallel excitation. *Magn Reson Med*. 2013;70:1210–1219.
67. Meliado EF, van den Berg CAT, Luijten PR, et al. Intersubject specific absorption rate variability analysis through construction of 23 realistic body models for prostate imaging at 7T. *Magn Reson Med*. 2019;81:2106–2119.
68. Gras V, Vignaud A, Amadon A, et al. Universal pulses: A new concept for calibration-free parallel transmission. *Magn Reson Med*. 2017;77:635–643.
69. Gras V, Mauconduit F, Vignaud A, et al. Design of universal parallel-transmit refocusing kT -point pulses and application to 3D T2 -weighted imaging at 7T. *Magn Reson Med*. 2018;80:53–65.
70. Hetherington HP, Avdievich NI, Kuznetsov AM, et al. RF shimming for spectroscopic localization in the human brain at 7 T. *Magn Reson Med*. 2010;63:9–19.
71. Li X, Auerbach EJ, Van de Moortele PF, et al. Quantitative single breath-hold renal arterial spin labeling imaging at 7T. *Magn Reson Med*. 2018;79:815–825.
72. Li P-FVdM X, Ugurbil K, Metzger G. Dynamically applied multiple B1+ shimming scheme for arterial spin labeling of the prostate at 7T. *Proc Intl Soc Mag Reson Med*. 2011;19:593.
73. Orzada S, Maderwald S, Poser BA, et al. RF excitation using time interleaved acquisition of modes (TIAMO) to address B1 inhomogeneity in high-field MRI. *Magn Reson Med*. 2010;64:327–333.
74. Orzada S, Maderwald S, Poser BA, et al. Time-interleaved acquisition of modes: an analysis of SAR and image contrast implications. *Magn Reson Med*. 2012;67:1033–1041.

75. Orzada S, Johst S, Maderwald S, et al. Mitigation of B1(+) inhomogeneity on single-channel transmit systems with TIAMO. *Magn Reson Med*. 2013;70:290–294.
76. Cloos MA, Knoll F, Zhao T, et al. Multiparametric imaging with heterogeneous radiofrequency fields. *Nat Commun*. 2016;7:12445.
77. Kalavagunta C, Michaeli S, Metzger GJ. In vitro Gd-DTPA relaxometry studies in oxygenated venous human blood and aqueous solution at 3 and 7 T. *Contrast Media Mol Imaging*. 2014;9:169–176.
78. Pintaske J, Martirosian P, Graf H, et al. Relaxivity of gadopentetate dimeglumine (Magnevist), gadobutrol (Gadovist), and gadobenate dimeglumine (MultiHance) in human blood plasma at 0.2, 1.5, and 3 Tesla. *Invest Radiol*. 2006;41:213–221.
79. Grobner T, Prischl FC. Gadolinium and nephrogenic systemic fibrosis. *Kidney Int*. 2007;72:260–264.
80. Kuo PH, Kanal E, Abu-Alfa AK, et al. Gadolinium-based MR contrast agents and nephrogenic systemic fibrosis. *Radiology*. 2007;242:647–649.
81. Kanda T, Fukusato T, Matsuda M, et al. Gadolinium-based contrast agent accumulates in the brain even in subjects without severe renal dysfunction: evaluation of autopsy brain specimens with inductively coupled plasma mass spectroscopy. *Radiology*. 2015;276:228–232.
82. Radbruch A, Weberling LD, Kieslich PJ, et al. Gadolinium retention in the dentate nucleus and globus pallidus is dependent on the class of contrast agent. *Radiology*. 2015;275:783–791.
83. von Morze C, Xu D, Purcell DD, et al. Intracranial time-of-flight MR angiography at 7T with comparison to 3T. *J Magn Reson Imaging*. 2007;26:900–904.
84. von Morze C, Purcell DD, Banerjee S, et al. High-resolution intracranial MRA at 7T using autocalibrating parallel imaging: initial experience in vascular disease patients. *Magn Reson Med*. 2008;26:1329–1333.
85. Schmitter S, Wu X, Adriany G, et al. Cerebral TOF angiography at 7T: Impact of B1 (+) shimming with a 16-channel transceiver array. *Magn Reson Med*. 2014;71:966–977.
86. Fortuin AS, Bruggemann R, van der Linden J, et al. Ultra-small superparamagnetic iron oxides for metastatic lymph node detection: back on the block. *Wiley Interdiscip Rev Nanomed Nanobiotechnol*. 2018;10:1–10.
87. Philips BWJ, Fortuin AS, Orzada S, et al. High resolution MR imaging of pelvic lymph nodes at 7 Tesla. *Magn Reson Med*. 2017;78:1020–1028.
88. Alon L, Deniz CM, Carluccio G, et al. Effects of anatomical differences on electromagnetic fields, SAR, and temperature change. *Concepts Magn Reson Part B Magn Reson Eng*. 2016;46:8–18.
89. Katscher U, Voigt T, Findeklee C, et al. Determination of electric conductivity and local SAR via B1 mapping. *IEEE Trans Med Imaging*. 2009;28:1365–1374.
90. Shrivastava D, Vaughan JT. A generic bioheat transfer thermal model for a perfused tissue. *J Biomech Eng*. 2009;131:074506.
91. Homann H, Bornert P, Eggers H, et al. Toward individualized SAR models and in vivo validation. *Magn Reson Med*. 2011;66:1767–1776.
92. Voigt T, Homann H, Katscher U, et al. Patient-individual local SAR determination: in vivo measurements and numerical validation. *Magn Reson Med*. 2012;68:1117–1126.
93. van Lier ALHMW, Raaijmakers A, Voigt T, et al. Electrical properties tomography in the human brain at 1.5, 3, and 7T: a comparison study. *Magn Reson Med*. 2014;71:354–363.
94. Alon L, Sodickson DK, Deniz CM. Heat equation inversion framework for average SAR calculation from magnetic resonance thermal imaging. *Bioelectromagnetics*. 2016;37:493–503.
95. Deniz CM, Alon L, Brown R, et al. Subject- and resource-specific monitoring and proactive management of parallel radiofrequency transmission. *Magn Reson Med*. 2016;76:20–31.
96. Murbach M, Neufeld E, Cabot E, et al. Virtual population-based assessment of the impact of 3 Tesla radiofrequency shimming and thermoregulation on safety and B1 + uniformity. *Magn Reson Med*. 2016;76:986–997.
97. Orzada S, Ladd ME, Bitz AK. A method to approximate maximum local SAR in multichannel transmit MR systems without transmit phase information. *Magn Reson Med*. 2017;78:805–811.
98. Eryaman Y, Lagore RL, Erturk MA, et al. Radiofrequency heating studies on anesthetized swine using fractionated dipole antennas at 10.5 T. *Magn Reson Med*. 2018;79:479–488.
99. ACR. Prostate Imaging – Reporting and Data System: PI-RADS V2. 2015. Available at: https://www.acr.org/-/media/ACR/Files/RADS/Pi-RADS/PIRADS-V2.pdf. Accessed January 15, 2019, 2019.
100. Lagemaat MW, Scheenen TW. Role of high-field MR in studies of localized prostate cancer. *NMR Biomed*. 2014;27:67–79.
101. Maas MC, Vos EK, Lagemaat MW, et al. Feasibility of T2 -weighted turbo spin echo imaging of the human prostate at 7 tesla. *Magn Reson Med*. 2014;71:1711–1719.
102. Vos EK, Lagemaat MW, Barentsz JO, et al. Image quality and cancer visibility of T2-weighted magnetic resonance imaging of the prostate at 7 Tesla. *Eur Radiol*. 2014;24:1950–1958.
103. Raaijmakers AJ, Luijten PR, van den Berg CA. Dipole antennas for ultrahigh-field body imaging: a comparison with loop coils. *NMR Biomed*. 2016;29:1122–1130.
104. Steensma BR, Luttje M, Voogt IJ, et al. Comparing signal-to-noise ratio for prostate imaging at 7T and 3T. *J Magn Reson Imaging*. 2019;49:1446–1455.
105. Wiggins G, Zhang B, Cloos MA, et al. Mixing loops and electric dipole antennas for increased sensitivity at 7 Tesla. *Proc Intl Soc Mag Reson Med*. 2013;21:2737.
106. Chen G, Laksshmanan K, Sodickson DK, et al. A combined electric dipole and loop head coil for 7T head imaging. *Proc Intl Soc Mag Reson Med*. 2015;23:3133.
107. Erturk MA, Raaijmakers AJE, Adriany G, et al. Comparison of 16-channel Stripline and 10-channel Fractionated Dipole Transceive Arrays for Body Imaging at 7T. *Proc Intl Soc Mag Reson Med*. 2015;23:3122.
108. Bitz AK, Klomp D, Ladd ME. Experimental and numerical determination of SAR and temperature distribution of a human endorectal coil for MR imaging of the prostate at 7T. *Proc Intl Soc Mag Reson Med*. 2008;16:903.
109. Lagemaat MW, Philips BW, Vos EK, et al. Feasibility of multiparametric magnetic resonance imaging of the prostate at 7 T. *Invest Radiol*. 2017;52:295–301.
110. Arteaga de Castro CS, van den Bergen B, Luijten PR, et al. Improving SNR and B1 transmit field for an endorectal coil in 7 T MRI and MRS of prostate cancer. *Magn Reson Med*. 2012;68:311–318.
111. Erturk MA, Tian J, Van de Moortele PF, et al. Development and evaluation of a multichannel endorectal RF coil for prostate MRI at 7T in combination with an external surface array. *J Magn Reson Imaging*. 2016;43:1279–1287.
112. Erturk A, Metzger GJ. Prostate MRI at 7.0 Tesla Using an Actively-Tuned Endorectal Coil. *Proc Intl Soc Mag Reson Med*. 2016;24:3501.
113. Klomp DW, Bitz AK, Heerschap A, et al. Proton spectroscopic imaging of the human prostate at 7 T. *NMR Biomed*. 2009;22:495–501.
114. Mescher M, Merkle H, Kirsch J, et al. Simultaneous in vivo spectral editing and water suppression. *NMR Biomed*. 1998;11:266–272.
115. Klomp DWJ, Scheenen TWJ, Arteaga CS, et al. Detection of fully refocused polyamine spins in prostate cancer at 7 T. *NMR Biomed*. 2011;24:299–306.
116. Lagemaat MW, Breukels V, Vos EK, et al. (1)H MR spectroscopic imaging of the prostate at 7T using spectral-spatial pulses. *Magn Reson Med*. 2016;75:933–945.
117. Swanson MG, Vigneron DB, Tabatabai ZL, et al. Proton HR-MAS spectroscopy and quantitative pathologic analysis of MRI/3D-MRSI-targeted postsurgical prostate tissues. *Magn Reson Med*. 2003;50:944–954.
118. Metzger GJ, Bolan P. Influence of contrast-dependent $T2^*$ effects on DCE-MRI of the prostate at 7T. *Proc Intl Soc Mag Reson Med*. 2009;17:5920.

119. Kobayashi N, Pang J, Moeller S, et al. Contrast Enhanced Self-Gated Coronary Angiography at 7 Tesla Using Ultra-Short Echo Time Imaging. *E-Poster presented at Proc Intl Soc Mag Reson Med; May; Toronto Ontario Canada*. 2015;23:2680.
120. Kobayashi N, Bolan PJ, Metzger GJ. Evaluation of UTE for improved contrast enhanced DCE MRI at 7T. *Oral presented at Proc Intl Soc Mag Reson Med; June; Paris France*. 2018;26:498.
121. Niendorf T, Graessl A, Thalhammer C, et al. Progress and promises of human cardiac magnetic resonance at ultrahigh fields: a physics perspective. *J Magn Reson*. 2013;229:208–222.
122. Rodgers CT, Piechnik SK, DelaBarre LJ, et al. Inversion recovery at 7 T in the human myocardium: measurement of T-1, inversion efficiency and B-1(+). *Magn Reson Med*. 2013;70:1038–1046.
123. Hezel F, Thalhammer C, Waiczies S, et al. High spatial resolution and temporally resolved $T2^*$ mapping of normal human myocardium at 7.0 Tesla: an ultrahigh field magnetic resonance feasibility study. *PLoS One*. 2012;7:e52324.
124. Huelnhagen T, Hezel F, Serradas Duarte T, et al. Myocardial effective transverse relaxation time $T2^*$ correlates with left ventricular wall thickness: a 7.0 T MRI study. *Magn Reson Med*. 2017;77:2381–2389.
125. Tao Y, Hess AT, Keith GA, et al. Optimized saturation pulse train for human first-pass myocardial perfusion imaging at 7T. *Magn Reson Med*. 2015;73:1450–1456.
126. Gregory TS, Cheng R, Tang GY, et al. The magnetohydrodynamic effect and its associated material designs for biomedical applications: a state-of-the-art review. *Adv Funct Mater*. 2016;26:3942–3952.
127. Chia JM, Fischer SE, Wickline SA, et al. Performance of QRS detection for cardiac magnetic resonance imaging with a novel vectorcardiographic triggering method. *J Magn Reson Imaging*. 2000;12:678–688.
128. Fischer SE, Wickline SA, Lorenz CH. Novel real-time R-wave detection algorithm based on the vectorcardiogram for accurate gated magnetic resonance acquisitions. *Magn Reson Med*. 1999;42:361–370.
129. Frauenrath T, Hezel F, Heinrichs U, et al. Feasibility of cardiac gating free of interference with electro-magnetic fields at 1.5 Tesla, 3.0 Tesla and 7.0 Tesla using an MR-stethoscope. *Invest Radiol*. 2009;44:539–547.
130. Frauenrath T, Hezel F, Renz W, et al. Acoustic cardiac triggering: a practical solution for synchronization and gating of cardiovascular magnetic resonance at 7 Tesla. *J Cardiovasc Magn Reson*. 2010;12:67.
131. Speier P, Fenchel M. R. R. PT-Nav: a novel respiratory navigation method for continuous acquisitions based on modulation of a pilot tone in the MR-receiver. *Proc European Society for Magnetic Resonance in Medicine and Biology*. 2015;32:128.
132. Schroeder L, Wetzl J, Maier A, et al. A novel method for contact-free cardiac synchronization using the pilot tone navigator. *Proc Intl Soc Mag Reson Med*. 2016;24:410.
133. Hess AT, Tunnicliffe EM, Rodgers CT, et al. Diaphragm position can be accurately estimated from the scattering of a parallel transmit RF coil at 7 T. *Magn Reson Med*. 2018;79:2164–2169.
134. Jaeschke SHF, Robson MD, Hess AT. Cardiac gating using scattering of an 8-channel parallel transmit coil at 7T. *Magn Reson Med*. 2018;80:633–640.
135. Bitz AK, Brote I, Orzada S, et al. Comparison of simulation-based and measurement-based RF shimming for whole-body MRI at 7 Tesla. *Proc Intl Soc Mag Reson Med*. 2010;18:4720.
136. Suttie JJ, Delabarre L, Pitcher A, et al. 7 Tesla (T) human cardiovascular magnetic resonance imaging using FLASH and SSFP to assess cardiac function: validation against 1.5 T and 3 T. *NMR Biomed*. 2012;25:27–34.
137. Setsompop K, Alagappan V, Gagoski B, et al. Slice-selective RF pulses for in vivo B1+ inhomogeneity mitigation at 7 tesla using parallel RF excitation with a 16-element coil. *Magn Reson Med*. 2008;60:1422–1432.
138. Brandts A, Westenberg JJ, Versluis MJ, et al. Quantitative assessment of left ventricular function in humans at 7 T. *Magn Reson Med*. 2010;64:1471–1477.
139. von Knobelsdorff-Brenkenhoff F, Frauenrath T, Prothmann M, et al. Cardiac chamber quantification using magnetic resonance imaging at 7 Tesla: a pilot study. *Eur Radiol*. 2010;20:2844–2852.
140. von Knobelsdorff-Brenkenhoff F, Tkachenko V, Winter L, et al. Assessment of the right ventricle with cardiovascular magnetic resonance at 7 Tesla. *J Cardiovasc Magn R*. 2013;15:23.
141. Prothmann M, von Knobelsdorff-Brenkenhoff F, Topper A, et al. High spatial resolution cardiovascular magnetic resonance at 7.0 tesla in patients with hypertrophic cardiomyopathy: first experiences: lesson learned from 7.0 tesla. *PLoS One*. 2016;11:e0148066.
142. Thalhammer C, Renz W, Winter L, et al. Two-dimensional sixteen channel transmit/receive coil array for cardiac MRI at 7.0 T: design, evaluation, and application. *J Magn Reson Imaging*. 2012;36:847–857.
143. Grassl A, Winter L, Thalhammer C, et al. Design, evaluation and application of an eight channel transmit/receive coil array for cardiac MRI at 7.0 T. *Eur J Radiol*. 2013;82:752–759.
144. Aussenhofer SA, Webb AG. An eight-channel transmit/receive array of TE01 mode high permittivity ceramic resonators for human imaging at 7T. *J Magn Reson*. 2014;243:122–129.
145. van Elderen SG, Versluis MJ, Webb AG, et al. Initial results on in vivo human coronary MR angiography at 7 T. *Magn Reson Med*. 2009;62:1379–1384.
146. van Elderen SG, Versluis MJ, Westenberg JJ, et al. Right coronary MR angiography at 7 T: a direct quantitative and qualitative comparison with 3 T in young healthy volunteers. *Radiology*. 2010;257:254–259.
147. Bizino MB, Bonetti C, van der Geest RJ, et al. High spatial resolution coronary magnetic resonance angiography at 7 T: comparison with low spatial resolution bright blood imaging. *Invest Radiol*. 2014;49:326–330.
148. Nezafat R, Stuber M, Ouwerkerk R, et al. B1-insensitive T2 preparation for improved coronary magnetic resonance angiography at 3 T. *Magn Reson Med*. 2006;55:858–864.
149. Huang F, Akao J, Vijayakumar S, et al. k-t GRAPPA: a k-space implementation for dynamic MRI with high reduction factor. *Magn Reson Med*. 2005;54:1172–1184.
150. Hoogduin JM, Raaijmakers A, Visser F, et al. Initial experience with BOLD imaging of the kidneys at 7T. *Proc Intl Soc Mag Reson in Med; May; Milan Italy*. 2014;22:456.
151. van Eijs MJM, van Zuilen AD, de Boer A, et al. Innovative perspective: gadolinium-free magnetic resonance imaging in long-term follow-up after kidney transplantation. *Front Physiol*. 2017;8:296.
152. Umutlu L, Orzada S, Kinner S, et al. Renal imaging at 7 Tesla: preliminary results. *Eur Radiol*. 2011;21:841–849.
153. Umutlu L, Kraff O, Orzada S, et al. Dynamic contrast-enhanced renal MRI at 7 Tesla: preliminary results. *Invest Radiol*. 2011;46:425–433.
154. Umutlu L, Maderwald S, Kinner S, et al. First-pass contrast-enhanced renal MRA at 7 Tesla: initial results. *Eur Radiol*. 2013;23:1059–1066.
155. Umutlu L, Maderwald S, Kraff O, et al. New look at renal vasculature: 7 tesla nonenhanced T1-weighted FLASH imaging. *J Magn Reson Imaging*. 2012;36:714–721.
156. Beiderwellen K, Kraff O, Laader A, et al. Contrast enhanced renal MR angiography at 7 Tesla: how much gadolinium do we need? *Eur J Radiol*. 2017;86:76–82.
157. Laader A, Beiderwellen K, Kraff O, et al. Non-enhanced versus low-dose contrast-enhanced renal magnetic resonance angiography at 7 T: a feasibility study. *Acta Radiol*. 2018;59:296–304.
158. Li X, Auerbach EJ, Van de Moortele PF, et al. Theoretical and experimental comparisons of single breath-hold renal perfusion imaging between 3T and 7T. *Power Poster presented at Proc Intl Soc Mag Reson Med; May; Toronto Ontario Canada*. 2015;23:759.
159. Hargreaves BA, Cunningham CH, Nishimura DG, et al. Variable-rate selective excitation for rapid MRI sequences. *Magn Reson Med*. 2004;52:590–597.

160. Hennig J, Scheffler K. Hyperechoes. *Magn Reson Med*. 2001;46:6–12.

161. Garwood M, DelaBarre L. The return of the frequency sweep: designing adiabatic pulses for contemporary NMR. *J Magn Reson*. 2001;153:155–177.

162. Li X, Van de Moortele PF, Ugurbil K, et al. Improved SNR at 7T for Non-Contrast Enhanced Cardiac Perfusion Imaging Using Arterial Spin Labeling. *EPoster presented at Proc Intl Soc Mag Reson Med; May; Milan Italy*. 2014;22:4921.

163. Li X, Metzger GJ. Feasibility of measuring prostate perfusion with arterial spin labeling. *NMR Biomed*. 2013;26:51–57.

164. Umutlu L, Bitz AK, Maderwald S, et al. Contrast-enhanced ultra-high-field liver MRI: a feasibility trial. *Eur J Radiol*. 2013;82:760–767.

165. Fischer A, Kraff O, Maderwald S, et al. Non-enhanced T1-weighted liver vessel imaging at 7 Tesla. *PLoS One*. 2014;9:e97465.

166. Laader A, Beiderwellen K, Kraff O, et al. 1.5 versus 3 versus 7 Tesla in abdominal MRI: a comparative study. *PLoS One*. 2017;12:e0187528.

167. Erturk MA, El-Sharkawy AM, Bottomley PA. Interventional loopless antenna at 7 T. *Magn Reson Med*. 2012;68:980–988.

168. Hoogendam JP, Kalleveen IM, de Castro CS, et al. High-resolution T2-weighted cervical cancer imaging: a feasibility study on ultra-high-field 7.0-T MRI with an endorectal monopole antenna. *Eur Radiol*. 2017;27:938–945.

169. Arteaga de Castro CS, Hoogendam JP, van Kalleveen IML, et al. Proton MRS of cervical cancer at 7 T. *NMR Biomed*. 2019;32:e4015.

170. Hahnemann ML, Kraff O, Maderwald S, et al. Non-enhanced magnetic resonance imaging of the small bowel at 7 Tesla in comparison to 1.5 Tesla: first steps towards clinical application. *Magn Reson Imaging*. 2016;34:668–673.

171. Hahnemann ML, Kraff O, Orzada S, et al. T1-weighted contrast-enhanced magnetic resonance imaging of the small bowel: comparison between 1.5 and 7 T. *Invest Radiol*. 2015;50:539–547.

172. Van de Moortele PF, Snyder C, DelaBarre L, et al. Fast Mapping of Relative B1+ Phase in the Human Head at 9.4 Tesla with a 14 Channel Transceive Coil Array. *Proc International Symposium on Biomedical Magnetic Resonance Imaging and Spectroscopy at Very High Fields Wurzburg Germany*. 2006.

173. Brunheim S, Gratz M, Johst S, et al. Fast and accurate multi-channel B1+ mapping based on the TIAMO technique for 7T UHF body MRI. *Magn Reson Med*. 2018;79:2652–2664.

174. Gras V, Boland M, Vignaud A, et al. Homogeneous non-selective and slice-selective parallel-transmit excitations at 7 Tesla with universal pulses: a validation study on two commercial RF coils. *PLoS One*. 2017;12:e0183562.

175. Guerin B, Setsompop K, Ye H, et al. Design of parallel transmission pulses for simultaneous multislice with explicit control for peak power and local specific absorption rate. *Magn Reson Med*. 2015;73:1946–1953.

176. Rietsch SHG, Brunheim S, Orzada S, et al. Development and evaluation of a 16-channel receive-only RF coil to improve 7T ultra-high field body MRI with focus on the spine. *Magn Reson Med*. 2019;82:796–810.

177. Brunheim S, Orzada S, Johst S, et al. 16-channel pTx body MRI for reduced field of view lumbar spine and kidney imaging at 7 Tesla. *Proc Intl Soc Mag Reson Med*. 2018;26:3393.

178. Orzada S, Bitz A, Gratz M, et al. A 32-channel transmit system add-on for 7 Tesla body imaging. *Proc Intl Soc Mag Reson Med*. 2017;25:1219.

179. Fiedler TM, Flöser M, Rietsch S, et al. Comparison of a 32-channel remote body coil for 7 Tesla with local and remote 8- and 16-channel transmit coil arrays. *Proc Intl Soc Mag Reson Med*. 2017;25:4306.

180. Orzada S, Maderwald S, Ohmigen M, et al. An 8-channel TX, 16-channel RX flexible body coil at 7 Tesla using both branches of centrally fed strip lines as individual receive elements. *Proc Intl Soc Mag Reson Med*. 2010;18:641.

181. Eryaman Y, Akin B, Atalar E. Reduction of implant RF heating through modification of transmit coil electric field. *Magn Reson Med*. 2011;65:1305–1313.

182. Eryaman Y, Guerin B, Akgun C, et al. Parallel transmit pulse design for patients with deep brain stimulation implants. *Magn Reson Med*. 2015;73:1896–1903.

183. Etezadi-Amoli M, Stang P, Kerr A, et al. Controlling radiofrequency-induced currents in guidewires using parallel transmit. *Magn Reson Med*. 2015;74:1790–1802.

184. Graesslin I, Krueger S, Vernickel P, et al. Detection of RF unsafe devices using a parallel transmission MR system. *Magn Reson Med*. 2013;70:1440–1449.